The Dynamics of Extratropical Oceanic Cyclones

by

JOHN RICHARD GYAKUM

B.S., Pennsylvania State University
(May, 1975)

Submitted in Partial Fulfillment
of the Requirements of the
Degree of

Master of Science

at the

Massachusetts Institute of Technology
(May, 1977)

Signature of Author.... .....
Department of Meteorology, May ,1977

Certified by.....
Thesis Supervisor

Accepted by.....
Chairman, Department Committee

The Dynamics of Extratropical Oceanic Cyclones

by

JOHN RICHARD GYAKUM

Submitted to the Department of Meteorology
on May 11, 1977 in partial fulfillment of the requirements
for the Degree of Master of Science.

ABSTRACT

A temperature structure appropriate for maritime areas is employed to find exact solutions to the non-linear quasi-geostrophic omega and vorticity equations, using a procedure similar to that used in a quasi-geostrophic model by Sanders (1971). Results are qualitatively similar to those found in the latter model, and thus, are consistent with the traditional baroclinic stability theory. The principal improvement in this new version is the finding that for intensifying storms, the cold tropospheric temperature perturbation also intensifies. This temperature perturbation is crucial to the storm intensification. Thus, we have a consistent physical mechanism which accounts for observed intensification of baroclinic waves. A frictional formulation is developed by solving for the frictionally induced vertical motion, and solving the vorticity equation, which includes both the effects of divergence and dissipation. A check on the validity of the frictional expression is made in connection with a simple thoery of thickness change over low centers. It is

found that the theory works well for land cases, thus, motivating us to use the theory for oceanic areas, where the density of data reports often precludes an accurate thickness analysis over an intense storm.

A large sampling of soundings from areas under the influence of intense maritime storms yielded little direct evidence of deep convection in those areas. However, it is speculated that convection may at times be an important factor in the fast evolution of maritime storms; the small space and time scales involved in convective processes may have precluded us from detecting any deep statically unstable layers. It is found by applying our sounding sample and diagnostic model to two cases of rapidly intensifying storms that our present model is not able to account for the observed rapid intensification.

Name and Title of Thesis Supervisor:

Professor Frederick Sanders

Professor of Meteorology

Acknowledgments

The author would like to express his deepest appreciation to Professor Sanders for suggesting the topic and offering helpful suggestions and assistance in both the work performed and in the preparation of the manuscript. Thanks are also due to Roy Jenne and Paul Mulder from NCAR for providing the radiosonde, ship, and satellite data, and also to the National Climatic Center in Asheville, North Carolia for copies of ships' logs. Much of the plotting and analysis work for our two storm cases was performed by Frank Colby. Thanks are also due to Miss Isabelle Cole for drafting the figures, and to Ms. Cheri Pierce for typing the final draft. Finally, many thanks are due to the author's parents, family, and friends for their constant moral support and encouragement. This research has been supported, in part, by NOAA Environmental Research Laboratories under Grant #04-5-022-9.

Table of Contents

	ABSTRACT	2
	ACKNOWLEDGMENTS	4
	TABLE OF CONTENTS	5
	LIST OF FIGURES AND TABLES	6
I.	Introduction	8
II.	The Diagnostic Model	10
	a. Vertical Motion	10
	b. Geopotential Tendency	22
	c. Intensification of the 1000 mb Low	26
	d. Motion of the Features	33
	e. Temperature Perturbation Tendency	48
	f. Frictional Effects	52
III.	Experiments with the Frictional Expression	60
IV.	The Sounding Sample	69
V.	Analysis Problem	81
VI.	A Further Look at the Sounding Samples	87
VII.	Application of the Model to the Two Oceanic Storm Cases	89
VIII.	Summary and Conclusions	93
	REFERENCES	96

List of Figures and Tables

Figure 1. Contributions to vertical motion for "Case C"..... 20

Figure 2a. The deepening rate $\hat{\mathcal{K}}_1(p_o)$ for $\hat{T}$ = 1°C..... 29

Figure 2b. " " " 30

Figure 3a. The zonal velocity component, C_{x_2}, for the 1000 mb center 35

Figure 3b. " " " 36

Figure 4. Values of the northward speed, C_{y_3}, for $\hat{T}$ = 1°C 39

Figure 5a. Ratio of C_{x_2} to the zonal component of the 500 mb wind 41

Figure 5b. " " " 42

Figure 6. Ratio of C_{y_3} to the meridional component of the 500 mb wind 43

Figure 7a. The eastward speed of the 250 mb trough and the overtaking rate $C_x(250) - C_{x_2}$ 45

Figure 7b. " " " 46

Figure 8a. The difference $[\hat{\mathcal{K}}_1(250) - \hat{\mathcal{K}}_1(1000)]$ for λ = L/4 49

Figure 8b. " " " 50

Figure 9. Frictional vertical velocity over the 1000 mb center 56

Figure 10a. Normalized square containing locations of soundings for "before" deepening 70

Figure 10b. Same as for 10a, except for "after" deepening 71

Figure 11a. Composite soundings for "before" deepening cases 72

Figure 11b. " " " 73

Figure 12a. Composite soundings for "after" deepening cases 74

Figure 12b. " " " 75

Figure 13a.	Mean soundings for "before" deepening cases.....	78
Figure 13b.	Mean soundings for "after" deepening cases	79
Table 1.	Calculated thickness changes over the low center	67
Table 2.	Values of the factor K (m/mb)	77
Table 3.	Calculated thickness change over the low center	85
Table 4.	Calculations of model parameters	90

I. Introduction

Intense extratropical oceanic cyclones directly affect the lives of relatively few of the world's inhabitants. Nevertheless, these storms form an essential part of such semipermanent meteorological features as the Aleutian and Icelandic lows, both of which account in part for the observed wind distribution in mid to high latitudes. They also play a crucial role, along with continental extratropical disturbances, in the necessary vertical and meridional transport of angular momentum and heat, as has been discussed by Palmen and Newton (1969). Rapid deepening is also observed to occur more frequently in maritime storms than in continental cyclones.

In order to examine some of the properties of these disturbances, we should like to examine the results of a structurally simple diagnostic model. Inspiration for such work comes from Sanders (1971). However, this latter model contains a temperature structure with a horizontal temperature gradient decreasing vertically from its maximum value at the surface to zero at the simulated tropopause level. Since we feel this represents an inadequate representation of temperature for maritime regions, we will use a more appropriate thermal structure. In addition, a larger range of effective vorticity stability will be used when we consider the selected properties of the model. Documentation for such a move will be made from an examination of the vertical structure of temperature and relative humidity in areas affected by intense oceanic storms. Due to the apparent importance of friction in the termination of deepening, a new formulation of surface friction effects will be discussed. Finally, we shall attempt to document the problem of

incorrect initial analysis with respect to oceanic cyclone intensification by examining two classic cases of explosive maritime storm development.

II. The Diagnostic Model

IIa. Vertical Motion

Following the procedure of Sanders (1971), we will assume that the flow is specified by the quasi-geostrophic vorticity equation

$$\frac{\partial \zeta}{\partial t} = -\underline{V} \cdot \nabla \eta + \eta_0 \frac{\partial \omega}{\partial p} \tag{1}$$

and by the thermodynamic equation

$$\frac{\partial}{\partial t}\left(\frac{\partial \phi}{\partial p}\right) = -\underline{V} \cdot \nabla \frac{\partial \phi}{\partial p} - \sigma(p)\omega \tag{2}$$

where ζ is the relative vorticity, η_0 is a constant value of the absolute vorticity, $\zeta + f$, ϕ is the geopotential, and the stability parameter $\sigma(p) = \left(d\phi/dp\right)\left(d\ln\theta/dp\right)$ is a function of pressure only. The relative vorticity, using the geostrophic relationship, may be expressed as

$$\zeta = \frac{\nabla^2 \phi}{f_0}$$

where f_0 is some constant value of the Coriolis parameter. Equation (1) now becomes

$$\nabla^2 \frac{\partial \phi}{\partial t} = -f_0 \underline{V} \cdot \nabla \eta + f_0 \eta_0 \frac{\partial \omega}{\partial p} \tag{3}$$

Combining equations (3) and (2) to eliminate $\frac{\partial \phi}{\partial t}$ now yields the w-equation.

$$\left(\nabla^2 + \frac{f_0^2 \gamma_0}{\sigma} \frac{\partial^2}{\partial p^2}\right) w = \frac{f_0}{\sigma} \frac{\partial}{\partial p}\left(\underline{V} \cdot \nabla \gamma\right) - \frac{1}{\sigma} \nabla^2 \left(\underline{V} \cdot \nabla \frac{\partial \phi}{\partial p}\right) \tag{4}$$

Using a structurally simple, yet realistic profile of temperature will allow us to solve equation (4).

We assume the following thermal structure:

$$T(x, y, p) = T_m(p) - \left(ay + \hat{T} \cos\frac{2\pi}{L} x \cos\frac{2\pi}{L} y\right) \tag{5}$$

where x and y axes are directed eastward and northward, respectively; a is the intensity of the meridional temperature gradient, and $\hat{T}$ represents the amplitude of the two-dimensional harmonic variation of temperature. This simplistic temperature profile does not lend itself to excessive mathematical complexity in the derivation of any forthcoming equations, and yet is quite realistic for extratropical maritime regions. Equation (5) indicates that the only variation of temperature in the vertical (with p as the vertical coordinate) is represented by the pressure dependence on the mean temperature for a given pressure level. Thus, there is no vertical variation of the horizontal temperature contrast. This is approximately true over much of the troposphere for oceanic regions. However, this temperature structure would extend to the top of the atmosphere, unless we specified a tropopause level, above which our temperature profile would be invalid. We shall specify this level by p_T, and disregard atmospheric processes above this

level. The price we would have to pay in attempting to realistically model stratospheric temperature (in the form of excessively complicated expressions) would presumably not be worth the additional physical insights to be gained from such an attempt. Indeed, allowing the temperature structure to stray unrealistically above the tropopause, just for the sake of defining the expression for all p, can prove to be potentially hazardous, as we shall later see.

The stability value σ is assumed to be a function of pressure only, and thus will be associated with T_m from expression (5). The definition of θ and σ, and the hydrostatic condition yields

$$\frac{d\ln\theta}{dp} = \left(\frac{d\ln T}{dp} - \frac{\kappa}{p}\right)$$

and

$$\sigma = \left(\frac{\kappa}{p} - \frac{d\ln T_m}{dp}\right)\frac{\kappa T_m}{p}$$

with $\kappa = R/c_p$.

Now, we define another stability parameter

$$\gamma = \kappa - p\,\frac{d\ln T_m}{dp}$$

where $\gamma = \kappa$ and $\gamma = 0$ correspond to isothermal and dry adiabatic lapse rates, respectively. With T_0 now chosen as a constant value of T_m, and γ being assumed independent of pressure, the expression for σ becomes

$$\sigma(p) = RT_0\gamma/p^2 \qquad (6)$$

The distribution of geopotential at $P=P_0=1000$ mb is given by

$$\phi(x,y,p_0) = \hat{\phi}_{10} \cos\frac{2\pi}{L}(x+\lambda)\cos\frac{2\pi}{L}y \qquad (7)$$

Here, λ represents the phase lag of the 1000 mb geopotential field with respect to the temperature field. A more complete explanation of λ and ϕ is given in a discussion of the original model (Sanders, 1971). Now for our "no-tropopause" case, or the horizontal temperature variation being independent of height:

$$\phi(x,y,p) = \phi(x,y,p_0) + \int_{p_0}^{p} \frac{\partial\phi}{\partial p}(x,y,p)\,dp$$

$$= \hat{\phi}_{10}\cos\frac{2\pi}{L}(x+\lambda)\cos\frac{2\pi}{L}y + \phi_m(p) - \left[R\ln\frac{p_0}{p}\left(ay + \hat{T}\cos\frac{2\pi}{L}x\cos\frac{2\pi}{L}y\right)\right] \qquad (8)$$

where

$$\phi_m(p) = \int_p^{1000} RT_m(p)\,d\ln p$$

and p is to be expressed in mb.

In order to construct an appropriate W-equation for this structurally simple model, we will represent the horizontal velocity $\underset{\sim}{V}$, geostrophically, as:

$$\underset{\sim}{V} = \frac{1}{f_0}\left(-\frac{\partial\phi}{\partial y}\underset{\sim}{i} + \frac{\partial\phi}{\partial x}\underset{\sim}{j}\right)$$

and the absolute vorticity

$$\eta = \frac{\nabla^2\phi}{f_0} + f$$

Using these relationships and the definitions of $\sigma(p)$ and $\phi(x,y,p)$, the w-equation (4) becomes

$$\left(\nabla^2+\frac{f_0^2\sigma_0}{RT_0\gamma}p^2\frac{\partial^2}{\partial p^2}\right)w=\left[\left(\frac{2\pi}{L}\right)^3\frac{R_a\hat{T}}{T_0\gamma}\left(\frac{\psi}{f_0}\right)p\ln\left(\frac{p_0}{p}\right)\right.$$

$$\left.+\left(\frac{2\pi}{L}\right)\frac{\hat{T}}{\gamma T_0}\left(\frac{\partial f}{\partial y}\right)_0 p\right]\sin\frac{2\pi}{L}x\cos\frac{2\pi}{L}y$$

$$-\left[\frac{\psi}{f_0}\left(\frac{2\pi}{L}\right)^3\frac{\hat{\phi}_{10}\,q}{\gamma T_0}p\right]\sin\frac{2\pi}{L}(x+\lambda)\cos\frac{2\pi}{L}y \qquad (9)$$

$$+\left[\frac{2}{f_0}\left(\frac{2\pi}{L}\right)^4\frac{\hat{\phi}_{10}\hat{T}}{T_0\gamma}\sin\left(\frac{2\pi}{L}\lambda\right)p\right]\sin\frac{4\pi}{L}y$$

We will use the β-plane approximation and regard $\left(\frac{\partial f}{\partial y}\right)_0$ as a constant. For example, $\left(\frac{\partial f}{\partial y}\right)_0=1.619\times10^{-11}\ m^{-1}\ sec^{-1}$ would correspond to a latitude of about 45°.

Because of this simplified temperature field, expression (9) is a good deal less complicated than the corresponding equation in the original model (see Sanders, 1971). However, the physical interpretation of the functions on the right side of (9) remains the same. The first term represents the vertical derivative of thermal vorticity advection due to the perturbed part of the temperature field by the portion of the thermal wind due to the basic north-south temperature gradient. The second portion of the first term involves the vertical derivative of the advection of earth vorticity by that part of the thermal wind due to the perturbed temperature gradient. The second term represents two identical effects in this model: the first being

the advection of the 1000 mb vorticity field by the thermal wind due to the meridional temperature gradient, and the second is due to the advection of this temperature field by the 1000 mb wind. The third and final term is the effect of the advection of the perturbed part of the temperature field by the 1000 mb wind.

The first term vanishes at the x-position of the temperature perturbation centers, while the second disappears at the x-position of the 1000 mb geopotential centers. The third term disappears when the 1000 mb center coincides with cold or warm pool centers ($\lambda = 0, 1/2$), at any y value corresponding to the latitude of the 1000 mb center ($y = 0$), or at the latitude where no 1000 mb meridional wind component exists ($y = 1/4$). Thus, it is evident that the only potential contribution to vertical motion over the 1000 mb center comes from the first term on the right-hand side of (9).

We shall now divide the solution of (9) into three parts, corresponding to the three forcing functions mentioned above:

$$\omega = \omega_1 + \omega_2 + \omega_3 \tag{10}$$

with the three parts of (9) as:

$$\left(\nabla^2 + \frac{f_0 \lambda_0 p^2}{R T_0 \gamma} \frac{\partial^2}{\partial p^2}\right) \omega_1 = \left[\left(\frac{2\pi}{L}\right)^3 \frac{R_d \hat{T}}{T_0 \gamma} \left(\frac{\psi}{f_0}\right) p \ln \frac{p_0}{p} - \left(\frac{2\pi}{L}\right) \frac{\hat{T}}{\gamma T_0} \left(\frac{\partial f}{\partial y}\right)_0 p\right] \sin \frac{2\pi}{L} x \cos \frac{2\pi}{L} y \tag{11a}$$

$$\left(\nabla^2 + \frac{f_0 h_0 p^2}{RT_0\gamma}\frac{\partial^2}{\partial p^2}\right)w_2 = -\left[\left(\frac{\psi}{f_0}\right)\left(\frac{2\pi}{L}\right)^3 \frac{\hat{\phi}_{10}\, q}{\gamma T_0}\, p\right]\sin\frac{2\pi}{L}(x+\lambda)\cos\frac{2\pi}{L}y \qquad (11b)$$

and

$$\left(\nabla^2 + \frac{f_0 h_0 p^2}{RT_0\gamma}\frac{\partial^2}{\partial p^2}\right)w_3 = \left[\frac{2}{f_0}\left(\frac{2\pi}{L}\right)^4 \frac{\hat{\phi}_{10}\,\hat{T}}{T_0\gamma}\sin\left(\frac{2\pi}{L}\lambda\right)p\right]\sin\frac{4\pi}{L}y \qquad (11c)$$

To find the solution, we require that each component of w have the same horizontal structure as its corresponding forcing function.

So

$$w_1 = \hat{w}_1(p)\sin\left(\frac{2\pi}{L}x\right)\cos\frac{2\pi}{L}y \qquad (12)$$

and

$$\nabla^2 w_1 = -2\left(\frac{2\pi}{L}\right)^2 w_1 = -2\left(\frac{2\pi}{L}\right)^2 \hat{w}_1 \sin\frac{2\pi}{L}x\cos\frac{2\pi}{L}y$$

Now, equation (11a) becomes

$$\left[\frac{f_0 h_0 p^2}{RT_0\gamma}\frac{\partial^2}{\partial p^2} - 2\left(\frac{2\pi}{L}\right)^2\right]\hat{w}_1 = \left[\left(\frac{2\pi}{L}\right)^3 \frac{Ra\hat{T}}{T_0\gamma}\left(\frac{\psi}{f_0}\right)p\ln\frac{p_0}{p} - \frac{2\pi}{L}\frac{\hat{T}}{\gamma T_0}\left(\frac{\partial f}{\partial y}\right)_0 p\right]\sin\left(\frac{2\pi}{L}x\right)\cos\frac{2\pi}{L}y \qquad (13)$$

Since equations (9) and (13) are second order equations, two boundary conditions are needed for w. We will require w, and each of its three components, to vanish at $P = P_0$, and $P = P_T$. P_T, as was

discussed earlier, is some specified pressure value of the tropopause. We shall ignore all vertical motion above P_T, because our assumed temperature structure makes no attempt to be realistic above this level. The computations performed in this paper will assume P_T = 250 mb, which is a bit below the traditional vertical motion vanishing level of 200 mb. This lower level is chosen to mitigate somewhat the effect of strong forcing aloft. The solution to equation (13) is, with these boundary conditions:

$$\hat{\omega}_1 = \hat{\omega}_{11} + \hat{\omega}_{12} \tag{14}$$

where

$$\hat{\omega}_{11} = \frac{k_{11} p}{b_1} \left\{ \frac{\left(p_0 \left(\frac{p}{p_T}\right)^{(q_1-1)} - p_T \left(\frac{p}{p_T}\right)^{(q_1-1)} \right) \frac{q_1}{b_1} + \left(\frac{p}{p_0}\right)^{(q_1-1)} p_T \ln\left(\frac{p_0}{p_T}\right)}{\left(p_0^{(1-q_1)} p_T^{q_1} - p_T^{(1-q_1)} p_0^{q_1} \right)} \right.$$

$$+ \frac{\frac{q_1}{b_1} \left(p_T \left(\frac{p_0}{p}\right)^{q_1} - p_0 \left(\frac{p_T}{p}\right)^{q_1} \right) - p_T \left(\frac{p_0}{p}\right)^{q_1} \ln\left(\frac{p_0}{p_T}\right)}{p_0^{(1-q_1)} p_T^{q_1} - p_T^{(1-q_1)} p_0^{q_1}}$$

$$\left. + \frac{q_1}{b_1} + \ln \frac{p}{p_0} \right\}$$

and

$$\hat{\omega}_{12} = \frac{k_{12} p}{b_1} \left\{ \frac{p_T \left(\frac{p}{p_0}\right)^{(q_1-1)} - p_0 \left(\frac{p}{p_T}\right)^{(q_1-1)} + p_0 \left(\frac{p_T}{p}\right)^{q_1} - p_T \left(\frac{p_0}{p}\right)^{q_1}}{p_T^{q_1} p_0^{(1-q_1)} - p_T^{(1-q_1)} p_0^{q_1}} - 1 \right\}$$

The values of the constants shown in the previous expressions are:

$$k_{11} = \left(\frac{2\pi}{L}\right)^3 \frac{R a \hat{T}}{b g} \left(\frac{\psi}{f_0}\right)$$

$$a_1 = \frac{f_0 \mathcal{N}_0}{R T_0 \gamma}$$

$$b_1 = 2\left(\frac{2\pi}{L}\right)^2$$

$$q_1 = \frac{1}{2} + \frac{1}{2}\sqrt{1 + 4\left(\frac{b_1}{a_1}\right)}$$

and

$$k_{12} = -\left(\frac{2\pi}{L}\right)\frac{\hat{T}}{\gamma T_0}\left(\frac{\partial f}{\partial \gamma}\right)_0$$

Proceeding in a similar manner to find the solutions to Equations (11b) and (11c), we have

$$w_2 = \hat{w}_2(p)\sin\frac{2\pi}{L}(x+\lambda)\cos\frac{2\pi}{L}y$$

and

$$w_3 = \hat{w}_3(p)\sin\frac{4\pi}{L}y$$

Subject to the same boundary conditions mentioned before, the expressions for $\hat{w}_2$ and $\hat{w}_3$ are

$$\hat{w}_2 = \frac{k_{21} p}{b_1}\left\{\frac{p_T\left(\frac{p}{p_0}\right)^{(q_1-1)} - p_0\left(\frac{p}{p_T}\right)^{(q_1-1)} + p_0\left(\frac{p_T}{p}\right)^{q_1} - p_T\left(\frac{p_0}{p}\right)^{q_1}}{\left(p_T^{q_1} p_0^{(1-q_1)} - p_T^{(1-q_1)} p_0^{q_1}\right)} - 1\right\} \qquad (15)$$

where

$$k_{21} = -\frac{4}{f_0}\left(\frac{2\pi}{L}\right)^3 \frac{\hat{\phi}_{10}\, a}{\gamma T_0}$$

and

$$\hat{\omega}_3 = \frac{k_{31}\, p}{b_2}\left\{\frac{p_T\left(\frac{p}{p_0}\right)^{(q_2-1)} - p_0\left(\frac{p}{p_T}\right)^{(q_2-1)} + p_0\left(\frac{p_T}{p}\right)^{q_2} - p_T\left(\frac{p_0}{p}\right)^{q_2}}{\left(p_T^{q_2} p_0^{(1-q_2)} - p_T^{(1-q_2)} p_0^{q_2}\right)} - 1\right\} \qquad (16)$$

where

$$k_{31} = \frac{2}{f_0}\left(\frac{2\pi}{L}\right)^4 \frac{\hat{\phi}_{10}\,\hat{T}}{T_0\,\gamma}\sin\left(\frac{2\pi}{L}\lambda\right)$$

$$b_2 = 4\left(\frac{2\pi}{L}\right)^2$$

and

$$q_2 = \frac{1}{2} + \frac{1}{2}\sqrt{1 + 4\left(\frac{b_2}{\sigma_1}\right)}$$

Each of the three components of ω corresponds to the appropriate forcing function on the right side of equation (9). Thus, the same physical processes are involved in the vertical motion components as are those processes described earlier involved with the forcing.

As a comparison to the vertical profile of $\hat{\omega}_1$, $\hat{\omega}_2$, and $\hat{\omega}_3$ found in "case C" of the original model (see figure 5 of Sanders, 1971), figure 1 shows these case C profiles for the revised model. A 250 mb tropopause was also simulated in the earlier model.

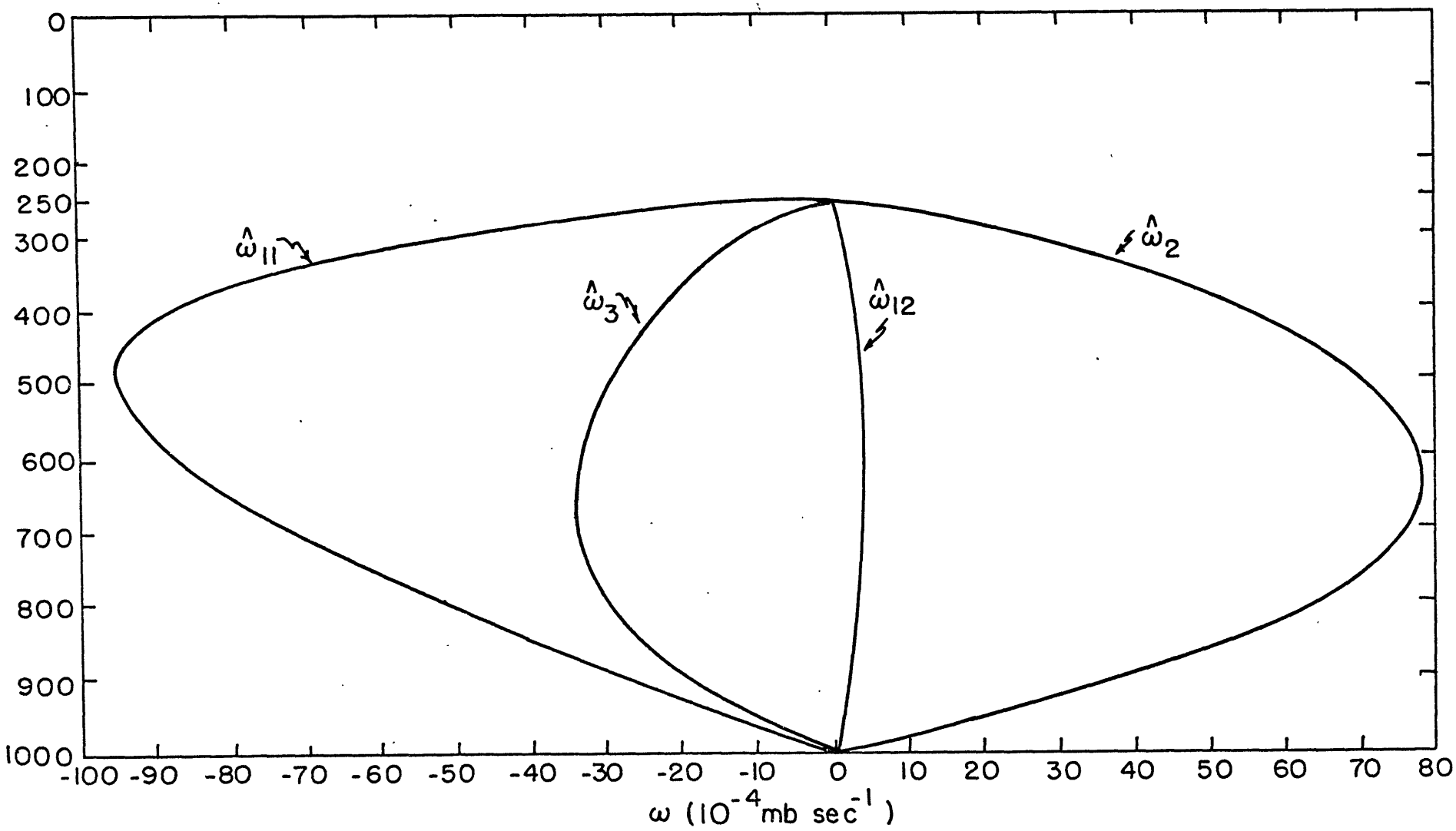

Fig. 1. Contributions to vertical motion for "case C". The values of various parameters are γ = .114, $f_o = \eta_o = 0.92 \times 10^{-4}$ sec^{-1}, T_o = 250° K, L = 2900 km, λ = L/4.

The general character of the profiles is preserved in both versions of the model. However, the maximum values of each of the w components is a good deal larger and occurs at higher levels than in the earlier version. The reason is that the temperature gradient does not damp out with height. Maximum values of w are located in the region of 500 to 650 mb in this model. It is interesting to see here how $\hat{w}_{11}$ (denoted " $k_{11}^w p_{11}^w$ " in the earlier version) is now the largest component, whereas $\hat{w}_{12}$ had the largest maximum value in the original model. The reason can be readily identified from the previous discussion of the physical factors involved in producing $\hat{w}_{11}$ and $\hat{w}_{12}$. $\hat{w}_{11}$ is dependent upon both the magnitude of the basic north-south temperature gradient and the temperature perturbation, while $\hat{w}_{12}$ is dependent only on the 1000 mb wind field and the meridional temperature gradient (not on the temperature perturbation).

As in the earlier model, w_1 gives tropospheric ascent from the cold trough to the downstream ridge, when $|\hat{w}_{11}| > |\hat{w}_{12}|$; w_2 yields ascent from the 1000 mb low to the mb high center, while w_3 shows ascent north of the temperature perturbation center and descent to the south, when $0 < \lambda < 1/2$. We shall later see that the dominance of $\hat{w}_{11}$ over $\hat{w}_{12}$ is crucial for the intensification of the low center.

While the action of vertical motion tends to be concentrated too much in the lower troposphere in the original model, our model probably tends to concentrate the vertical motion at levels too high in the troposphere for this continental storm case. However, because our temperature structure is likely to be more accurate for maritime cases, we should expect these higher maximum values of vertical motion for oceanic cases.

IIb. Geopotential Tendency

Suitable expressions for the geopotential tendency $\chi = \frac{\partial \phi}{\partial t}$ may be found by solving the vorticity equation (3). This may be accomplished by finding the vorticity advection using equation (8), and evaluating the divergence term by differentiating the expression for w, equation (10).

The vorticity equation now becomes

$$\nabla^2 \chi = f_1(p) \sin\left(\frac{2\pi}{L}x\right)\cos\left(\frac{2\pi}{L}y\right) + f_2(p) \sin\frac{2\pi}{L}(x+\lambda)\cos\frac{2\pi}{L}y + f_3(p)\sin\frac{4\pi}{L}y \tag{17}$$

where f_1, f_2, and f_3 are simply pressure dependent functions found as coefficients of the appropriate harmonic term when deriving the above equation.

We shall divide the solution into three parts, just as the solution to the w-equation was divided

$$\chi = \chi_1 + \chi_2 + \chi_3 \tag{18}$$

with

$$\nabla^2 \chi_1 = f_1(p) \sin\left(\frac{2\pi}{L}x\right)\cos\left(\frac{2\pi}{L}y\right)$$

$$\nabla^2 \chi_2 = f_2(p) \sin\frac{2\pi}{L}(x+\lambda)\cos\frac{2\pi}{L}y$$

and

$$\nabla^2 \chi_3 = f_3(p)\sin\frac{4\pi}{L}y$$

As before, we assume that each component of the solution have the same horizontal structure as its corresponding forcing function, so that

$$\psi_1 = \hat{\psi}_1 \sin\frac{2\pi}{L}x \cos\frac{2\pi}{L}y$$

$$\psi_2 = \hat{\psi}_2 \sin\frac{2\pi}{L}(x+\lambda) \cos\frac{2\pi}{L}y$$

$$\psi_3 = \hat{\psi}_3 \sin\frac{4\pi}{L}y$$

where

$$\hat{\psi}_1 = -f_1(p)\Big/_{2\left(\frac{2\pi}{L}\right)^2} = -f_1(p)\Big/_{b_1}$$

$$\hat{\psi}_{12} = -f_2(p)\Big/_{b_1}$$

and

$$\hat{\psi}_3 = -f_3(p)\Big/_{b_2}$$

The evaluation of the f(p) terms yields

$$\hat{\psi}_1 = \hat{\psi}_{11} + \hat{\psi}_{12} + \hat{\psi}_{13} \tag{19}$$

where

$$\hat{\psi}_{11} = -\frac{1}{b_1}\left(\frac{2\pi}{L}\right) R\hat{T}\left(\ln\frac{p_0}{p}\right)\left[\frac{2}{f_0}\left(\frac{2\pi}{L}\right)^2 R_d\left(\ln\frac{p_0}{p}\right) - \left(\frac{\partial f}{\partial y}\right)_0\right]$$

$$\hat{\gamma}_{12} = -\frac{4\eta_0}{b_1^2}\left(\frac{2\pi}{L}\right)^3 \frac{Ra\hat{T}}{T_0\gamma}\left\{\frac{\left[p_0 q_1\left(\frac{p}{p_T}\right)^{(q_1-1)} - p_T q_1\left(\frac{p}{p_0}\right)^{(q_1-1)}\right]\frac{q_1}{b_1} + q_1\left(\frac{p}{p_0}\right)^{(q_1-1)} p_T \ln\left(\frac{p_0}{p_T}\right)}{\left(p_0^{(1-q_1)} p_T^{q_1} - p_T^{(1-q_1)} p_0^{q_1}\right)}\right.$$

$$+ \frac{\frac{q_1}{b_1}\left[(1-q_1) p_T\left(\frac{p_0}{p}\right)^{q_1} - (1-q_1) p_0\left(\frac{p_T}{p}\right)^{q_1}\right] - (1-q_1) p_T\left(\frac{p_0}{p}\right)^{q_1} \ln\left(\frac{p_0}{p_T}\right)}{\left(p_0^{(1-q_1)} p_T^{q_1} - p_T^{(1-q_1)} p_0^{q_1}\right)}$$

$$\left. + \frac{q_1}{b_1} + \ln\frac{p}{p_0} + 1\right\}$$

and

$$\hat{\gamma}_{13} = \frac{f_0\eta_0}{b_1^2}\left(\frac{2\pi}{L}\right)\frac{\hat{T}}{\gamma T_0}\left(\frac{\partial f}{\partial \gamma}\right)_0\left[f_{13}(p)\right]$$

where $$f_{13}(p) = \left\{\frac{p_T q_1\left(\frac{p}{p_0}\right)^{(q_1-1)} - p_0 q_1\left(\frac{p}{p_T}\right)^{(q_1-1)} + p_0(1-q_1)\left(\frac{p_T}{p}\right)^{q_1} - p_T(1-q_1)\left(\frac{p_0}{p}\right)^{q_1}}{\left(p_T^{q_1} p_0^{(1-q_1)} - p_T^{(1-q_1)} p_0^{q_1}\right)} - 1\right\}$$

$$\hat{\gamma}_2 = \hat{\gamma}_{21} + \hat{\gamma}_{22} \qquad (20)$$

where

$$\hat{\gamma}_{21} = -\frac{1}{b_1}\left[\hat{\phi}_{10}\left(\frac{2\pi}{L}\right)\left(\frac{\partial f}{\partial \gamma}\right)_0 - \left(\frac{2}{f_0}\right)\left(\frac{2\pi}{L}\right)^3 \hat{\phi}_{10} Ra\left(\ln\frac{p_0}{p}\right)\right]$$

and

$$\hat{\gamma}_{22} = \frac{4\eta_0}{b_1^2}\left(\frac{2\pi}{L}\right)^3 \frac{\hat{\phi}_{10}\, q}{\gamma T_0}\left[f_{13}(p)\right]$$

and

$$\hat{\gamma}_3 = \hat{\gamma}_{31} \qquad (21)$$

where $$\tilde{\chi}_{31} = -\frac{\eta_0 \hat{\phi}_{10} \hat{T}}{8 T_0 \gamma} \sin\left(\frac{2\pi}{L}x\right)$$

$$\times\left[\frac{p_T q_2 \left(\frac{p}{p_0}\right)^{(q_2-1)} - p_0 q_2 \left(\frac{p}{p_T}\right)^{(q_2-1)} + p_0(1-q_2)\left(\frac{p_T}{p}\right)^{q_2} - p_T(1-q_2)\left(\frac{p_0}{p}\right)^{q_2}}{\left(p_T q_2 p_0^{(1-q_2)} - p_T^{(1-q_2)} p_0 q_2\right)} - 1\right]$$

An examination of the structure of the previous terms indicates that $\hat{\chi}_{11}$ and $\hat{\chi}_{21}$ are both directly due to vorticity advection with the remaining components resulting directly from horizontal divergence. Of course, the horizontal divergence due to w_1 is indirectly forced by vorticity advection. Since vorticity advection effects are generally negligible at 1000 mb, the divergence represents the critical mechanism for the deepening of a 1000 mb center. Since the only vertical motion found over a geopotential center in this model is that due to w_1, negative divergence in the lower tropopause associated with this quantity deepens the low. Thus, when a low is located between a cold trough and the downstream warm ridge, ascent in this region due to w_1 intensifies the low (ignoring frictional effects). As was discussed earlier, $\hat{w}_{11}$ (the ascent term downstream of the cold trough to the warm ridge) dominates $\hat{w}_{12}$ (descent in the same region) to effect this deepening.

IIc. Intensification of the 1000 mb Low

If we consider the deepening rate of the 1000 mb low, where $x=\frac{1}{2}-\lambda$, $y=0$, $p=p_0$, equation (18) becomes

$$\mathfrak{I}_1\left(\frac{L}{2}-\lambda, 0, p_0\right) = \hat{\mathfrak{I}}_1(p_0)\sin\left(\frac{2\pi\lambda}{L}\right) \tag{22}$$

Thus, as with the previous model, maximum deepening occurs when $\lambda=L/4$, and the deepening vanishes when the low is located at either the cold or warm perturbation centers.

In our model,

$$\hat{\mathfrak{I}}_1(p_0) = \frac{-\eta_0 R a \hat{T}}{\left(\frac{2\pi}{L}\right) T_0 \gamma}\left\{\frac{\left[(1-2q_1)+q_1\left(\frac{p_0}{p_T}\right)^{q_1}+(1-q_1)\left(\frac{p_0}{p_T}\right)^{(1-q_1)}\right]\frac{q_1}{b_1}-(1-2q_1)\ln\left(\frac{p_0}{p_T}\right)}{\left(\frac{p_0}{p_T}\right)^{(1-q_1)}-\left(\frac{p_0}{p_T}\right)^{q_1}}\right.$$

$$\left. + \frac{q_1}{b_1}+1\right\} \tag{23}$$

$$+\frac{f_0\eta_0\hat{T}}{4\left(2\pi/L\right)^3 T_0\gamma}\left(\frac{\partial f}{\partial y}\right)_0\left\{\frac{(2q_1-1)-q_1\left(\frac{p_0}{p_T}\right)^{q_1}+(1-q_1)\left(\frac{p_0}{p_T}\right)^{(1-q_1)}}{\left(\frac{p_0}{p_T}\right)^{(1-q_1)}-\left(\frac{p_0}{p_T}\right)^{q_1}}-1\right\}$$

A "case C" calculation made with equation (23) was found to be $\hat{\mathfrak{I}}_1(p_0) = -2.05\times10^{-4}\ m^2/sec^3$, or a deepening rate for sea-level pressure of about -12.0 mb $(12\ hr)^{-1}$. This compares with an observed deepening of -8 mb, but we have not yet considered frictional filling. Our value for $\hat{\mathfrak{I}}_1(p_0)$ is slightly greater in magnitude than the number which would be found in the original model, even when we amplify a and $\hat{T}$ each by a factor of 4/3 to account for the original model

temperature structure in the 100 - 500 mb layer. No such amplification factor is needed in the present model, because we have assumed no variation of horizontal temperature gradient with height. The reason is, of course, the enhanced forcing in the form of the temperature gradients in the upper troposphere. The physical interpretation of each of the terms in equation (23) is the same as the terms found in equation (29) of Sanders' work (1971). Both terms arise from the divergence due to w_1. The first term on the right side of (23) arises from relative vorticity advection, while the second acts as a result of the advection of earth vorticity. The first term is the active deepening mechanism for a 1000 mb low placed between a cold trough and a downstream warm ridge, for it produces ascent in this region; while the second term acts as a brake on the deepening process by causing descent in this same area.

Why does the active deepening mechanism have a greater effect with respect to the brake in this version of the model than in the first version? The answer is that the first term is much more dependent on the temperature gradient magnitudes (both meridional and pertubed) than is the second term, which depends only on the perturbed temperature gradient strength (the value $\hat{T}$). However, there is still the same superficial exponent dependence on L, as in the earlier version, such that the braking action of the second term will increase more rapidly than the increase of the first term with higher values of L. Thus, we should expect a limiting value of wavelength, beyond which no net intensification will occur. The importance of such L-dependent parameters as b_1 and q_1 in (23) remains obscure, but is likely to be

small. Thus, discounting this latter consideration, we should expect generally higher wavelengths of maximum deepening, due to the lessened effectiveness of the braking term. We can also perceive this fact with the knowledge that since the vertical scale of the baroclinicity is larger in this model, the preferred horizontal scale is also larger in this model. Equation (23) also shows that a meridional temperature gradient is required for deepening, while $\hat{\zeta}_1(p_0)$ is directly proportional to the magnitudes of $\hat{T}$ and the vorticity-stability parameter $\left(\frac{\gamma_0}{T_0\gamma}\right)$.

Figure 2 confirms and summarizes the previous statements. It also indicates that the wavelength of maximum deepening range from 1500 to 5000 km. The wavelength of maximum instability (assuming $\hat{\zeta}_1$ is an indication of the instability of the baroclinic system) decreases with increasing values of the vorticity-stability value, corresponding with the observationally inspired notion that smaller stability favors intensification of smaller storms.

The range of both a and the vorticity-stability value are extended in this and forthcoming charts from the ranges used in the reported results of the earlier version of the model (see Sanders, 1971). The upward limit of a is extended to 30°C/100 km, because the values found in experiments conducted in a synoptic lab class at M.I.T. go beyond the previous upper limit of 2°C/100 km. A maximum value of the vorticity-stability parameter of 11.2 x $10°C^{-1}$ sec^{-1} is chosen on the basis of a high value of $\eta = 2f$ (area averaged), T_o = 250°, and $\gamma = .071$. This latter value is taken from the least stable saturated sounding (with respect to the moist adiabat) of a sample of radiosonde observations (mainly weather ships and island stations) in regions under the

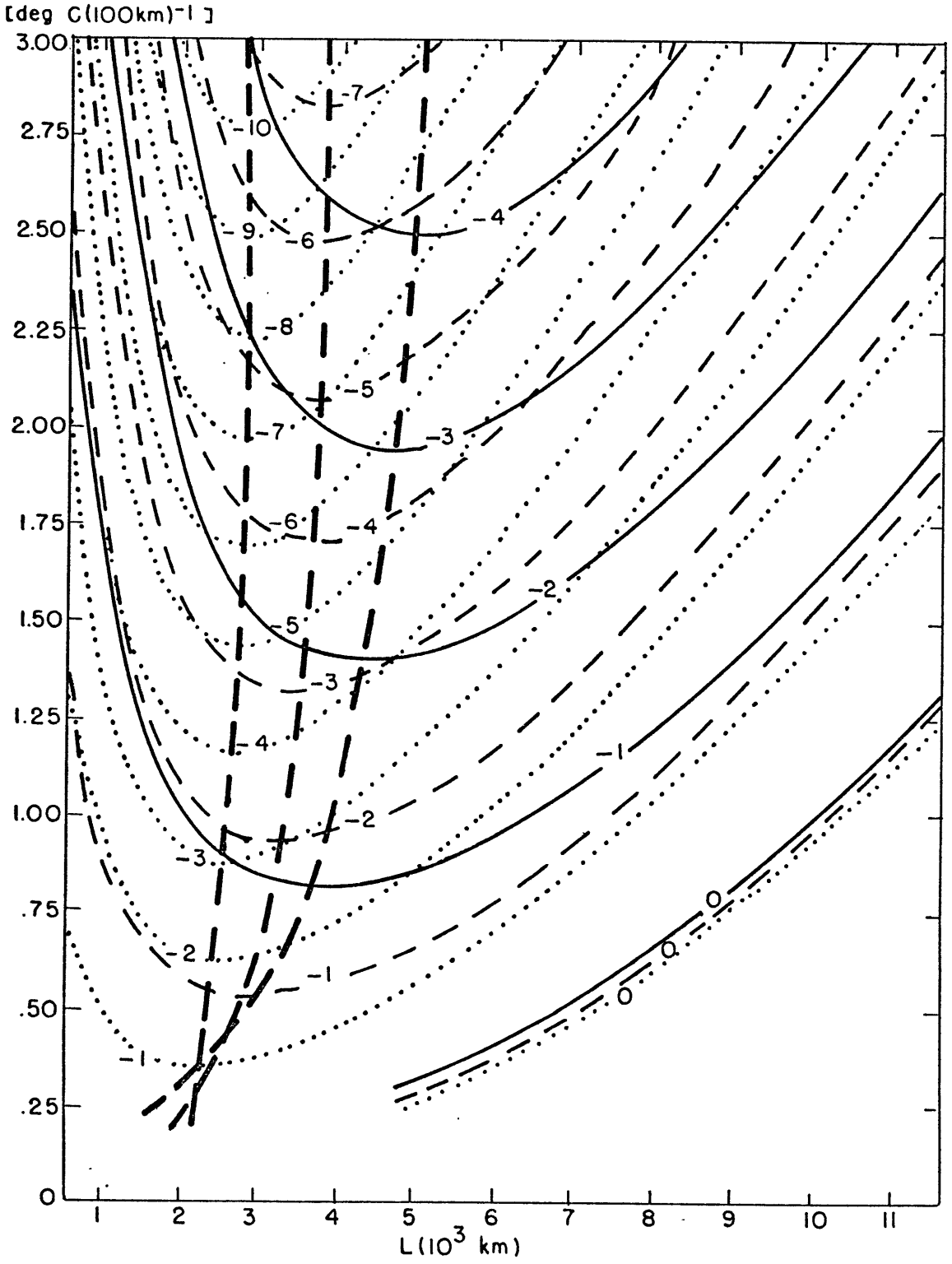

Fig. 2a. The deepening rate $\hat{\chi}_1(p_s)$ for $\hat{T} = 1^{\circ}C$ as a function of the wavelength and the meridional temperature gradient. The units are $10^{-3} m^2 sec^{-3}$. The heavy solid, heavy dashed, and dotted lines in Fig. A indicate values of the vorticity-stability parameter of 1.4,2.8, and 5.6×10^{-6} sec^{-1} $^{o}K^{-1}$. Part B shows for vorticity-stability values of 5.6,8.4, and 11.2×10^{-6} sec^{-1} $^{o}K^{-1}$ for the dotted, lightly dashed,

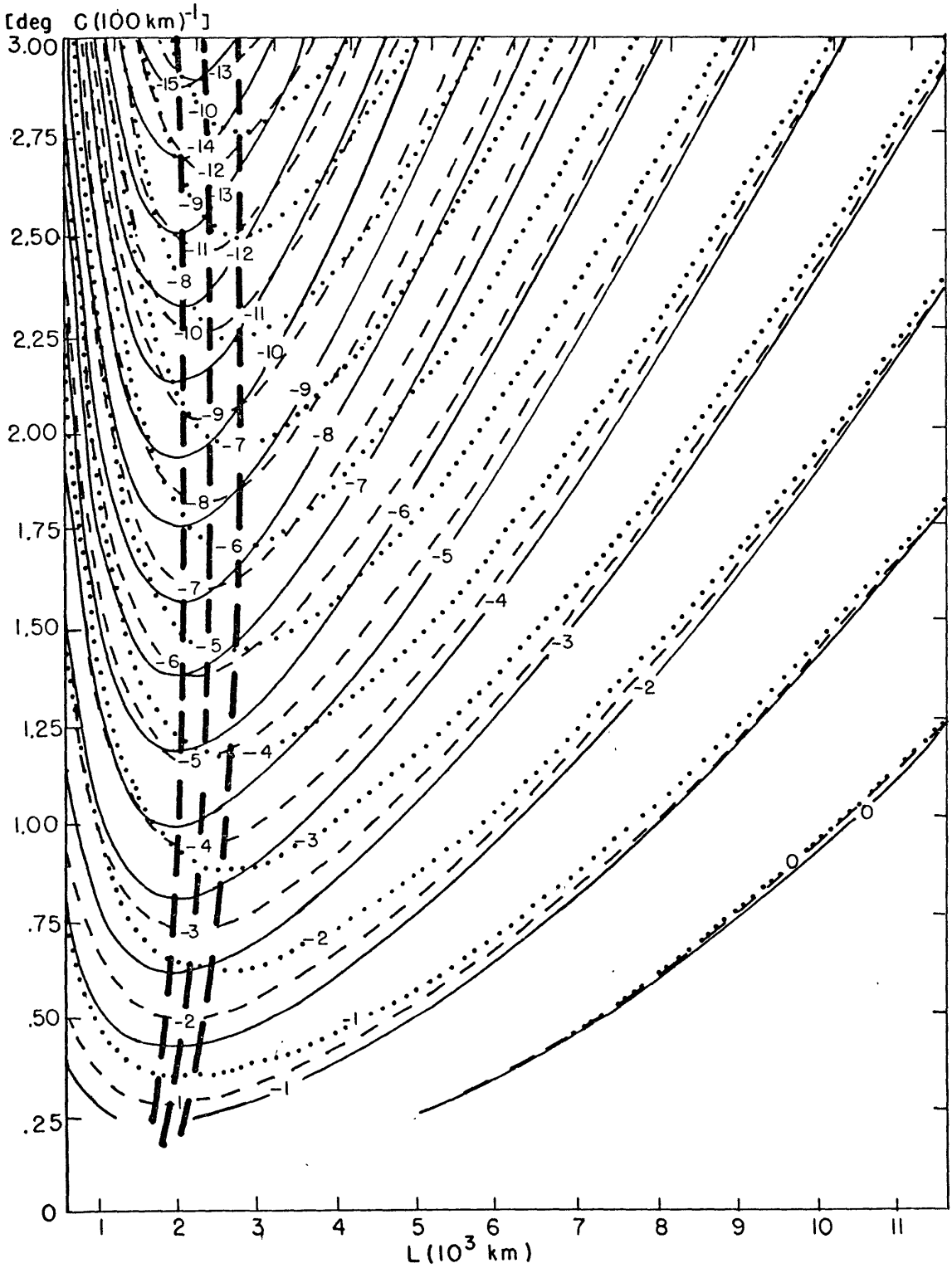

Fig. 2b. and lightly solid lines, respectively. The extra heavy dashed lines connecting the troughs of the isopleths are the loci of the wavelength of maximum deepening.

influence of intense oceanic storms. Due to our previous assumption of γ being independent of height, this stability value necessarily is based on a deep layer. Temperature differences between 850 and 500 mb are used in determining γ. Thus, boundary layer effects and vertical temperature differences above 500 mb are not considered. Latent heat of condensation can be taken into account in saturated layers, if the vertical temperature difference is compared to the vertical temperature difference along the appropriate moist adiabat. Therefore, the extension of the vorticity-stability parameter to higher values represents an attempt to consider the effectively lowered static stabilities when the air is saturated. This consideration will hopefully lead the model to capture some of the explosive development which is so frequent over maritime regions. A more complete discussion of the stability sampling is contained in a later section of this paper.

One further note concerning the notion of a longwave cutoff is added here. An original attempt to define a temperature field of the form

$$T(x,y,p) = T_m(p) - \left(1-\alpha^2\left(\ln\frac{p_0}{p}\right)^2\right)\left(dy + \hat{T}\cos\left(\frac{2\pi}{L}x\right)\cos\left(\frac{2\pi}{L}y\right)\right) \qquad (24)$$

was used to specify still another set of model equations. Equation (24) shows that the magnitude of the temperature gradients do not damp out as much with height in the troposphere as do the gradients in the original model. However, the price paid for such a benefit was an even more unrealistic stratospheric temperature profile in the form of excessively large horizontal temperature gradients. The upper boundary condition to the ω-equation was $\omega = 0$ at $p = 0$, as in the original version of the

model; these latter two effects brought on an unrealistic ω_1 profile (especially in the stratosphere), and, thus, potentially spurious χ_1 values. This latter event manifested itself at 1000 mb, and was readily seen when a chart of the form of figure 2 was constructed. We found that for increasing values of the vorticity-stability parameter, contamination from excessive forcing from the region of the atmosphere above the tropopause increased so that a longwave cutoff for deepening no longer existed. At $\left(\lambda_0/\gamma T_0\right)$ values high enough (say, at $\lambda_0/\gamma T_0$ = $2.8 \times 10^{-6}\,^{\circ}C^{-1}\ sec^{-1}$), the deepening rate actually increased with wavelength, apparently without limit.

This trend is even evident in Sanders' figure 13 (1971), but not nearly so much because the excessive forcing is not as great. Contamination appears at wavelengths greater than 6000 km by virtue of the slope of the lines decreasing with increasing values of $\lambda_0/T_0\gamma$. Presumably, if the values of χ_1 were computed for much higher (and beyond the range observed in the real atmosphre) values of the vorticity-stability parameter, no preferred wavelength for instability would appear, as in the situation described above.

IId. Motion of the Features

It is of interest to examine the motion of the geopotential features. We need simply use Petterssen's (1956) formulas to evaluate the motion. The eastward speed may be written as

$$c_x(p) = \frac{\partial \zeta / \partial x}{\partial^2 \phi / \partial x^2}\left(x_T, 0, p\right) \tag{25}$$

The position of the trough axis, X_T, may be found by looking for the minimum value of geopotential ϕ (x, y, p), along the y = 0 axis. The solution is

$$X_T(p) = \left(\frac{L}{2\pi}\right) \tan^{-1}\left[\frac{\hat{\phi}_{10} \sin\left(\frac{2\pi}{L}\lambda\right)}{R\hat{T}\ln\left(\frac{p_0}{p}\right) - \hat{\phi}_{10}\cos\left(\frac{2\pi}{L}\lambda\right)}\right] \tag{26}$$

where X_T is between x = 0 and x = $(L/2) - \lambda$, the position of the 1000 mb low. We may now find an expression for $c_x(p)$, with a knowledge of X_T, by differentiating our expression for ζ once and the one for ϕ (x, y, p) twice, so that

$$c_x(p) = \frac{\hat{\zeta}_1(p)\cos\left(\frac{2\pi}{L}x_T\right) + \hat{\zeta}_2(p)\cos\frac{2\pi}{L}\left(x_T + \lambda\right)}{\left(2\pi/L\right)\left[\hat{\phi}_{10}\cos\frac{2\pi}{L}(x_T+\lambda) - R\hat{T}\ln\left(\frac{p_0}{p}\right)\cos\left(\frac{2\pi}{L}x_T\right)\right]} \tag{27}$$

For the motion of the 1000 mb low center, equation (27) may be expressed as

$$c_x(p_0) = c_{x_1}\cos\left(\frac{2\pi}{L}\lambda\right) + c_{x_2} \tag{28}$$

where c_{x1} and c_{x2} represent the effects of χ_1 and χ_2, respectively:

$$c_{x1} = \frac{\chi_1(p_0)}{\left(\frac{2\pi}{L}\right)\hat{\phi}_{10}} \tag{29}$$

and

$$c_{x2} = \frac{\lambda_0 a}{\left(\frac{2\pi}{L}\right)^2 \gamma T_0}\left[\frac{q_1 - q_1\left(\frac{p_0}{p_T}\right)^{q_1} + \left(1-q_1\right)\left(\frac{p_0}{p_T}\right)^{(1-q_1)} - (1-q_1)}{\left(\frac{p_0}{p_T}\right)^{(1-q_1)} - \left(\frac{p_0}{p_T}\right)^{q_1}} - 1\right] - \frac{1}{2\left(\frac{2\pi}{L}\right)^2}\left(\frac{\partial f}{\partial y}\right)_0 \tag{30}$$

For our sample case, the values of c_{x2} and c_{x1} in this version of the model are 17.4 m/sec and 9.3 m/sec, respectively. This compares with c_{x2} = 13.7 m/sec and c_{x1} = 4.7 m/sec in the old version. The observed 12 hour displacement rate was 11 m/sec, showing the new calculations as being too fast. The parameter c_{x1} is still smaller than c_{x2}, but represents a relatively greater significance with respect to c_{x2} than in the old formulation. The reason is the new temperature profile enhances χ_1 more than χ_2. c_{x1} has no effect if the low is located so that $\lambda = L/4$, as happens in our sample case C. The physical effect of c_{x1} is the same in this model version; it will retard eastward speed for warm lows and enhance it for $L/4 < \lambda < L/2$. Since c_{x1} has a potentially significant effect in the model, accurate placement of the low (to determine λ) is crucial in determining this effect.

Figure 3 shows the eastward speed of the 1000 mb center as a function of wavelength and meridional temperature gradient. The maximum

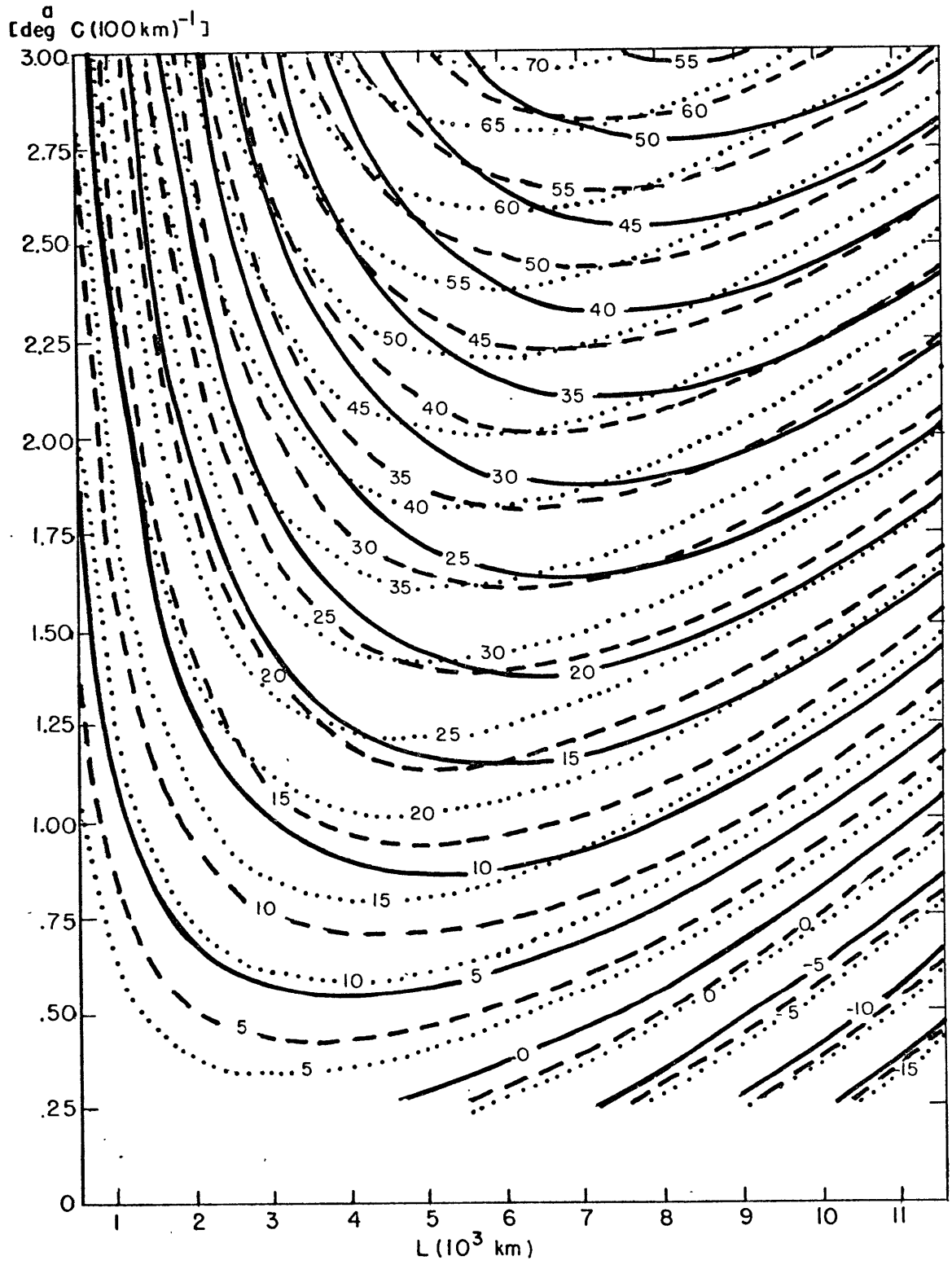

Fig. 3a. The zonal velocity component, C_{x2}, for the 1000mb center as a function of wavelength, and meridional temperature gradient for selected values of vorticity-stability. The isotachs indicate units of meters per second and are positive values for eastward displacement. The correspondence of the solid, dashed, and dotted lines in each part of the figure are as explained in figure 2.

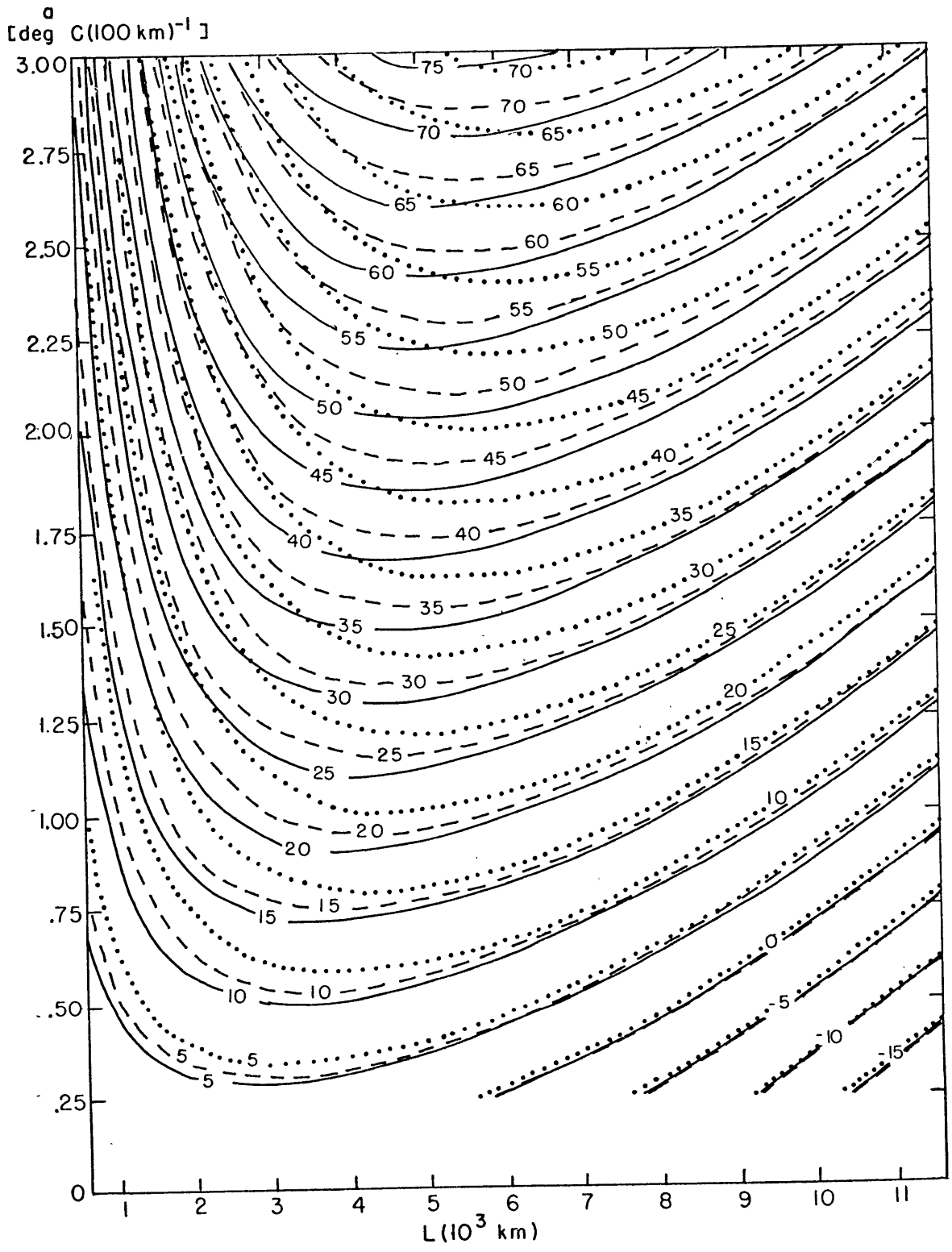

Fig. 3b. Same as for part A, except for vorticity-stability values of 5.6 , 8.4, and 11.2 sec^{-1} ^{o}K.

values of this motion are found in the wavelength range from 2500 km to 8000 km - somewhat higher than the wavelengths found in Sanders' figure 10 (1971). Also, generally higher westerly values for a given vorticity-stability parameter, wavelength, and a value are observed in this formulation. Increasing magnitudes of eastward movement are found with increasing vorticity-stability numbers and increasing a values. The wavelength of maximum speed decreases with increasing values of vorticity-stability , just as the wavelength of maximum deepening decreases with higher magnitudes of vorticity-stability. The reader should be cautioned to watch out for the effect of C_{x1} , particularly when the temperature perturbation is intense; because the magnitude of C_{x1} is direclty proportional to $\hat{T}$.

The meridional component of motion may be obtained by using Petterssen's formula:

$$C_y(p_0) \simeq \frac{-\partial \chi / \partial y}{\partial^2 \phi_{10} / \partial y^2} \left(L/2 - \lambda, 0, p_0 \right) \tag{31}$$

so that

$$C_y(p_0) = C_{y3} \sin\left(\frac{2\pi}{L}\lambda\right) \tag{32}$$

where C_{y3} is due to $\hat{\chi}_3(p_0)$ and

$$C_{y3} = \frac{\gamma_0 \hat{T}}{4\left(\frac{2\pi}{L}\right)^2 \Gamma_0 \gamma} \left[\frac{q_2 - q_2\left(\frac{p_0}{p_T}\right)^{q_2} + (1-q_2)\left(\frac{p_0}{p_T}\right)^{(1-q_2)} - (1-q_2)}{\left(\frac{p_0}{p_T}\right)^{(1-q_2)} - \left(\frac{p_0}{p_T}\right)^{q_2}} - 1 \right]$$

Since c_{y_3} is generally a positive term, geopotential centers have a northward component of motion when located between the cold trough and its downstream warm ridge. The case C value of c_{y_3} is 10.2 m/sec, compared with the earlier model value of 9.1 m/sec, and an observed 12 hour displacement rate of 7.5 m/sec.

Figure 4 shows values of c_{y_3} for $\hat{T}$ = 1°C as a function of vorticity-stability and wavelength. The magnitude of c_{y_3} is proportional to the magnitude of $\hat{T}$, and independent of the basic meridional temperature gradient. The main difference between this figure and Sanders' figure 11 (1971) is that values for larger values of vorticity-stability are given here. There is a slight increase of c_{y_3} over corresponding values in the earlier version, for given values of L and $\left(h_0/T_0\delta\right)$.

A comparison of the motion of the low center with the flow aloft at 500 mb is appropriate. We have seen that the zonal motion of the 1000 mb low (c_{x_2}) is due to the divergence of ω_2, which is forced by the meridional temperature gradient; while the meridional displacement of the feature is due to the divergence of ω_3, which is forced by the temperature perturbation gradient. Although the contours of the 500 mb pattern are associated hydrostatically with the above temperature patterns in the 1000 - 500 mb layer, a direct steering relationship between the flows at 500 mb and the 1000 mb low is not clear.

The components of the 500 mb flow over the low center are

$$u_s = -\left(\frac{1}{f_0}\right)\frac{\partial \phi}{\partial y}\left(L/2 - \lambda, 0, 500\ mb\right)$$

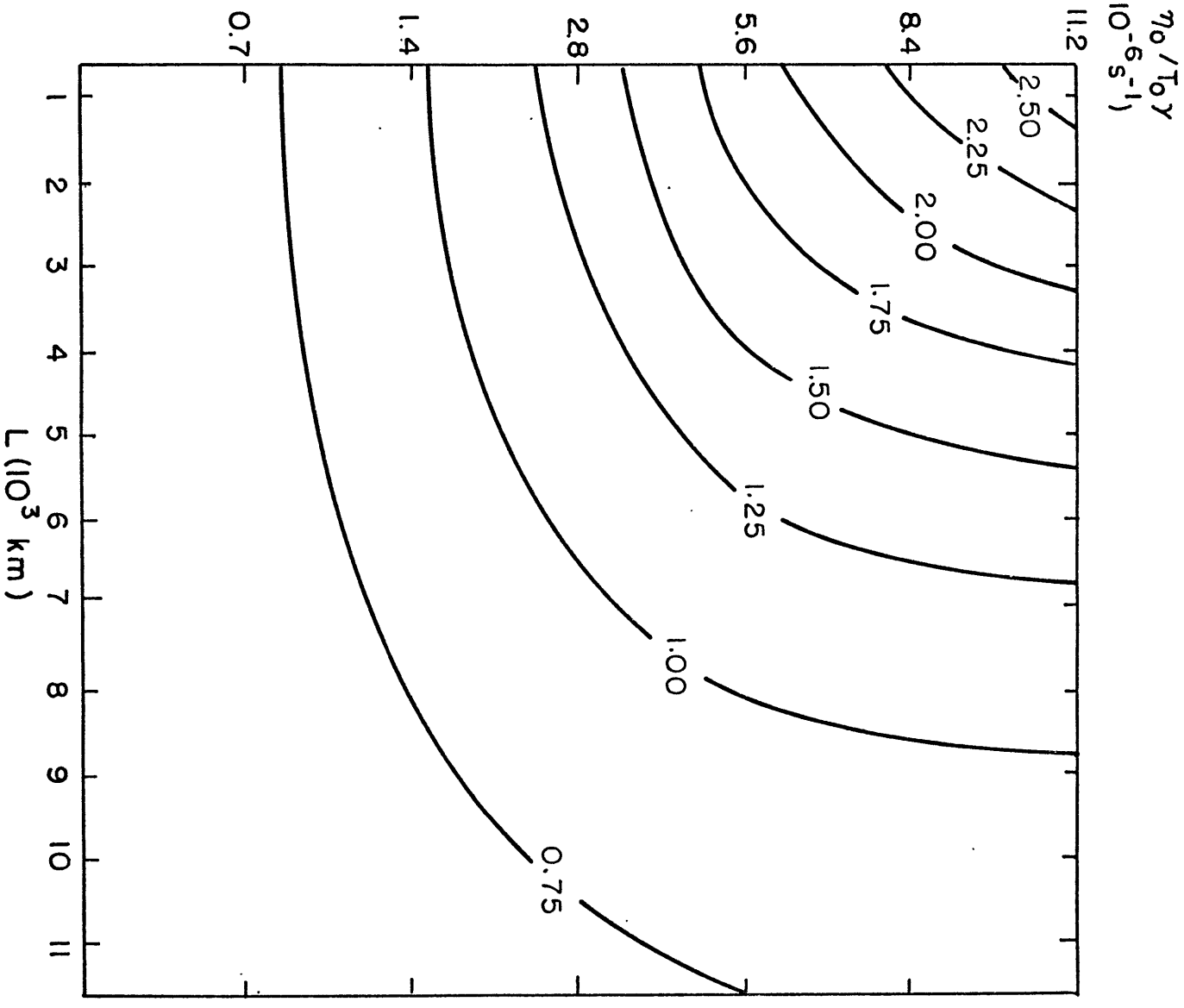

Fig. 4. Values of the northward speed, C_{y3} as a function of vorticity-stability value and the wavelength for $\bar{T}$ = 1 °C. The isotach labels are in units of meters per second.

$$V_5 = \left(\frac{1}{f_0}\right)\frac{\partial \phi}{\partial x}\ \left(\lambda = \lambda, 0, 500\ mb.\right)$$

From our definition of ϕ (x, y, p), equation (8), and for $\lambda = L/4$

$$u_5 = \frac{R_d \ln(2)}{f_0} \tag{33}$$

$$V_5 = \frac{R\hat{T}}{f_0}\left(\frac{2\pi}{L}\right)\ln(2) \tag{34}$$

For case C, we find values of U_5 = 24.1 m/sec and V_5 = 33.8 m/sec. The values of C_{x_2} and C_{y_3} are 17.4 m/sec and 10.2 m/sec, respectively. Thus, the low is moving at a speed of 20.2 m/sec toward 060° while the 500 mb flow is 41.5 m/sec toward 035°. When a comparison is made with the earlier version of the model, we see that the low is moving somewhat more to the right of this 500 mb flow in this version. The speeds of both the 500 mb flow and the low are greater in this model (20.2 m/sec versus 16 m/sec for the low, and 41.5 m/sec versus 31.2 m/sec at 500 mb), due primarily to the enhanced temperature gradients aloft.

The relationship between the 500 mb flow and the 1000 mb system movement is shown in Figures 5 and 6. The ratio C_{x_2}/U_5 has maximum values at wavelengths between 2500 km and 8000 km for a given value of $\underline{a}$, and for the indicated vorticity-stability range. Also, for given values of a, $\nu_0/\gamma T_0$, and L, C_{x_2}/U_5 tends to be slightly higher than in the previous model. Values of C_{y_3}/V_5, which is independent of both a and $\hat{T}$, are found in figure 6. Aside

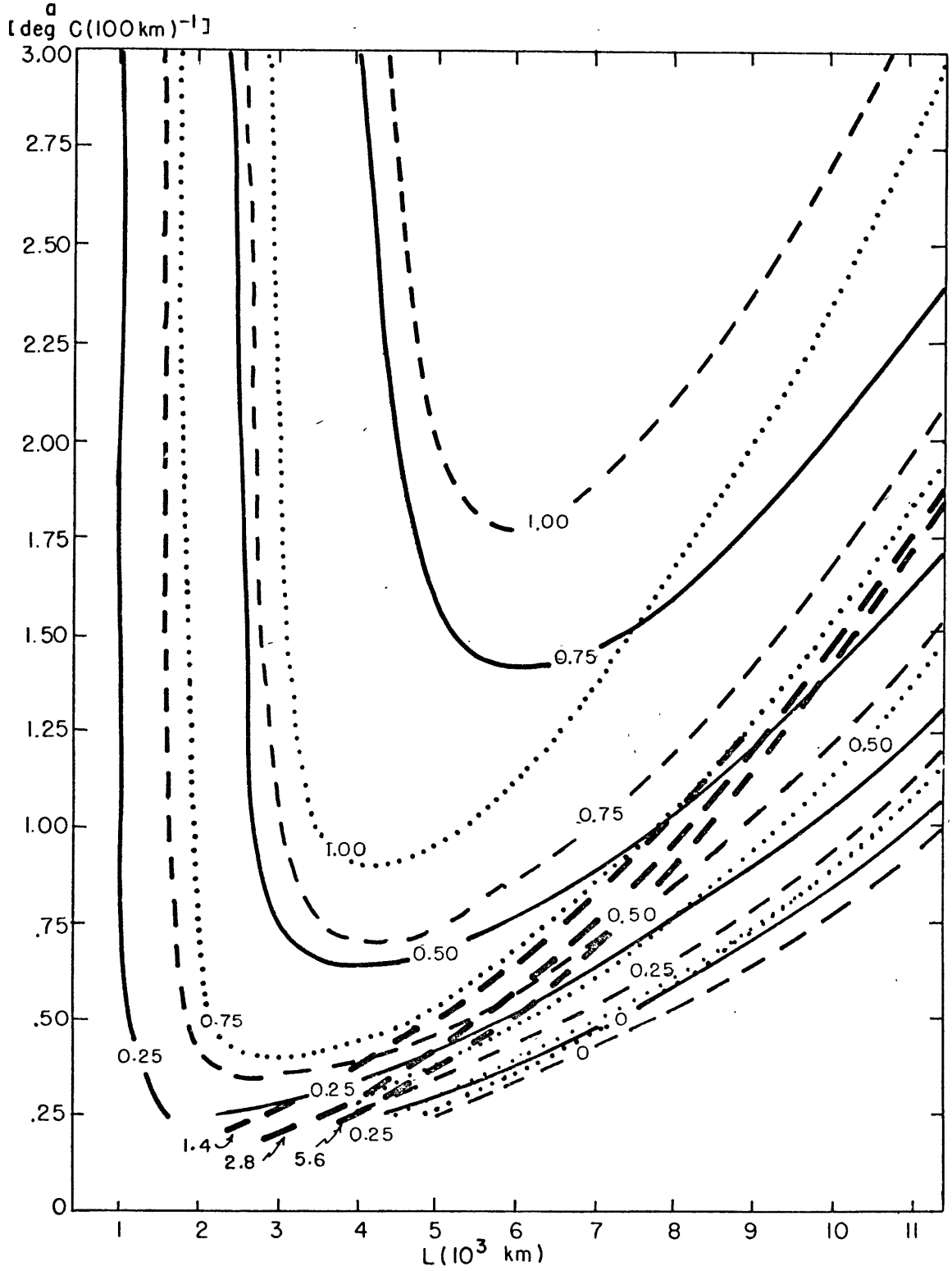

Fig. 5a. Ratio of C_{x2} to the zonal component of the 500mb wind as a function of meridional temperature gradient and wavelength. The solid, dashed, and dotted lines in each part are as indicated in Fig. 2. The heavy dashed lines indicate the loci of wavelength, beyond which the 1000mb low moves to the left of the upper level flow.

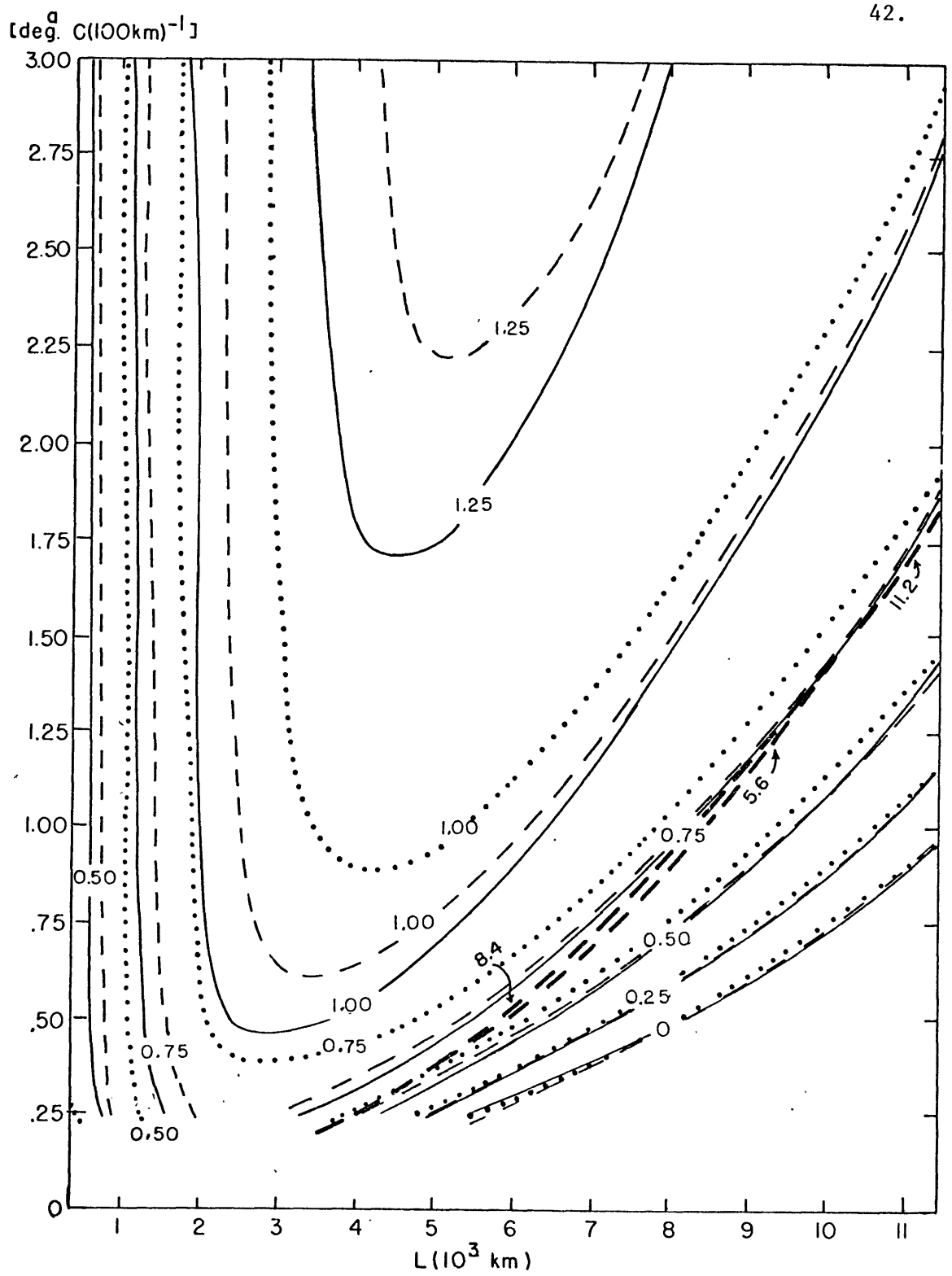

Fig. 5b. Same as for 5a, except for vorticity-stability values of 5.6, 8.4, and 11.2 sec^{-1} $^oK^{-1}$.

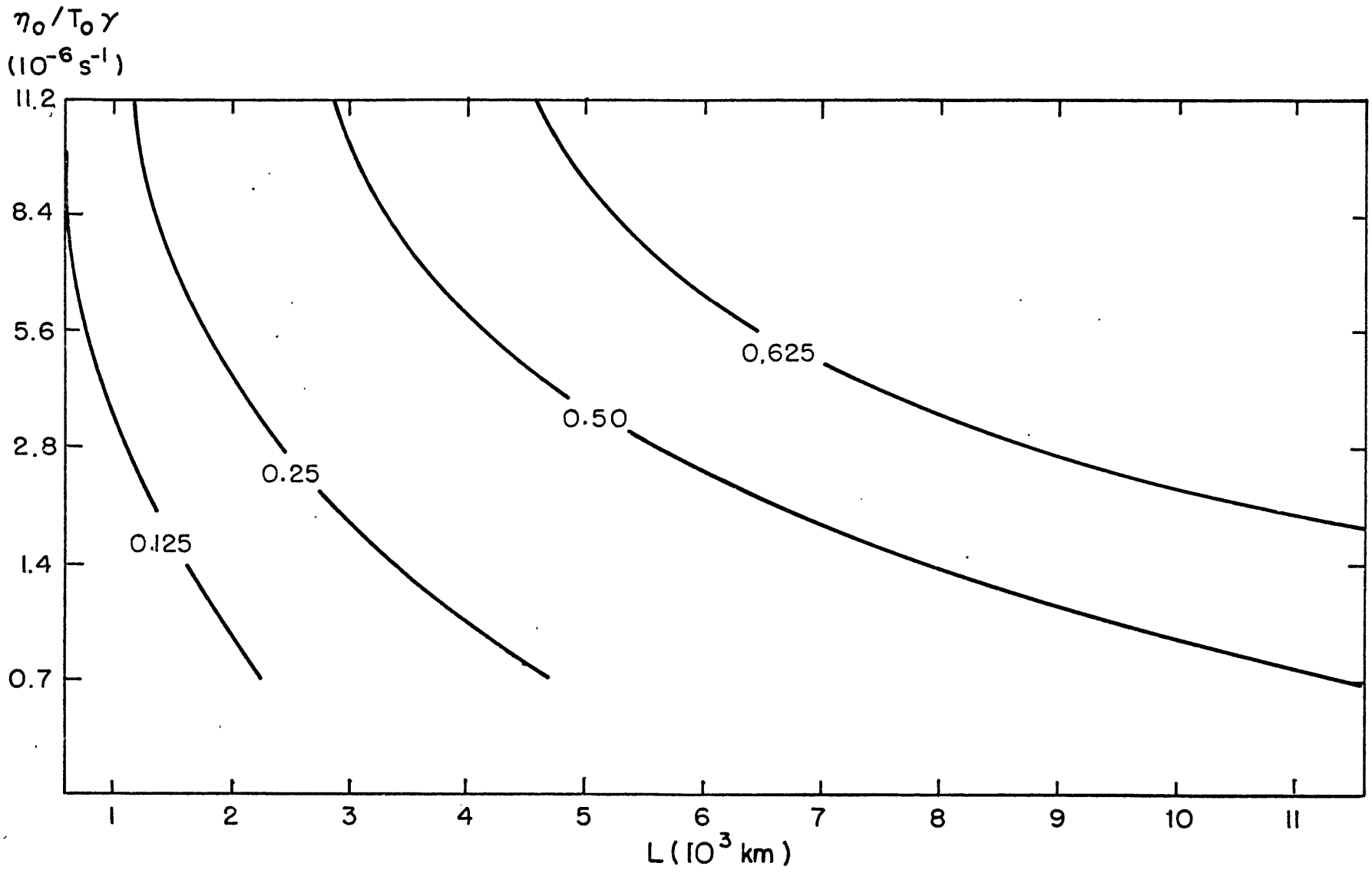

Fig. 6. Ratio of C_{y3} to the meridional component of the 500mb wind as a function of wavelength and vorticity-stability value.

from the extension of the range of vorticity-stability values, little change from Sanders' figure 12 (1971) is indicated. We see in figure 5 that the conditions under which lows move to the right of the 500 mb flow are those under which most storms are observed to occur (for $\lambda = L/4$, the low moves to the right of the 500 mb contour when $c_{x_1}/u_s > c_{y_2}/v_s$). Indeed, a somewhat wider range of conditions under which this movement occurs is found in this model. As in the earlier model, both the 500 mb flow and the motion of the low approach the zonal direction when the surface feature is located at either of the temperature perturbation centers.

Since the 1000 - 500 mb thickness pattern is shaped in a similar fashion to the 500 mb pattern, the theoretical and observed motions of surface lows generally moving to the right of the 500 mb flow indicate that they also move toward warmer air. However, this does not mean that the low is warming, because the adiabatic ascent over the cyclone acts to oppose the warm air ingestion of the storm. The topic of thickness change following the low center will be discussed in a later section.

We shall now examine a possible clue as to the extent that occlusion takes place in the model. If the 250 mb trough were overtaking the surface low, the cold perturbation would presumably be doing likewise; thus, occlusion would be occurring. Since the zonal speed of 250 mb trough is a complicated function of all the model parameters (see equations 26 and 27), figure 7 shows the results of calculations for $\bar{T}$ = 5°C, $\hat{\phi}_{10}$ = 10^3 m^2 sec^{-2}, and with $\eta_0/\gamma T_0$ = 2.8×10^{-6} °C^{-1} sec^{-1} and $\eta_0/\gamma T_0$ = 11.2×10^{-6} °C^{-1} sec^{-1}. Part A

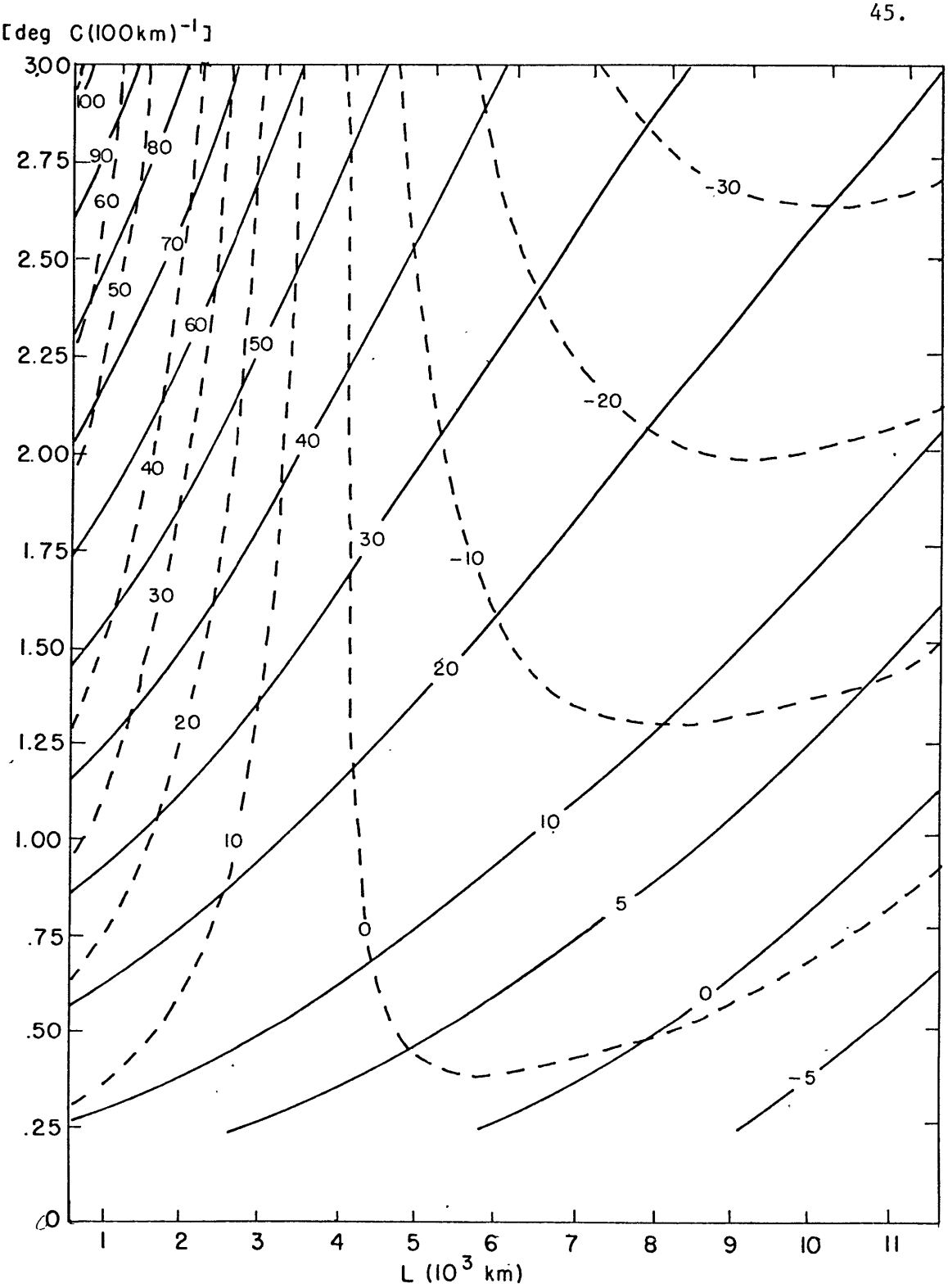

Fig. 7a. The eastward speed of the 250mb trough is indicated by the solid lines, while the dashed lines indicate the overtaking rate, $C_x(250) - C_{x2}$, as a function of meridional temperature gradient and wavelength. Part A of the fig. is for $\gamma_o/T_o\,\gamma = 2.8 \times 10^{-6}\,\mathrm{sec}^{-1}\,{}^{o}\mathrm{K}^{-1}$, $\hat{T} = 5\,{}^{o}\mathrm{C}$, and $\lambda = L/4$.

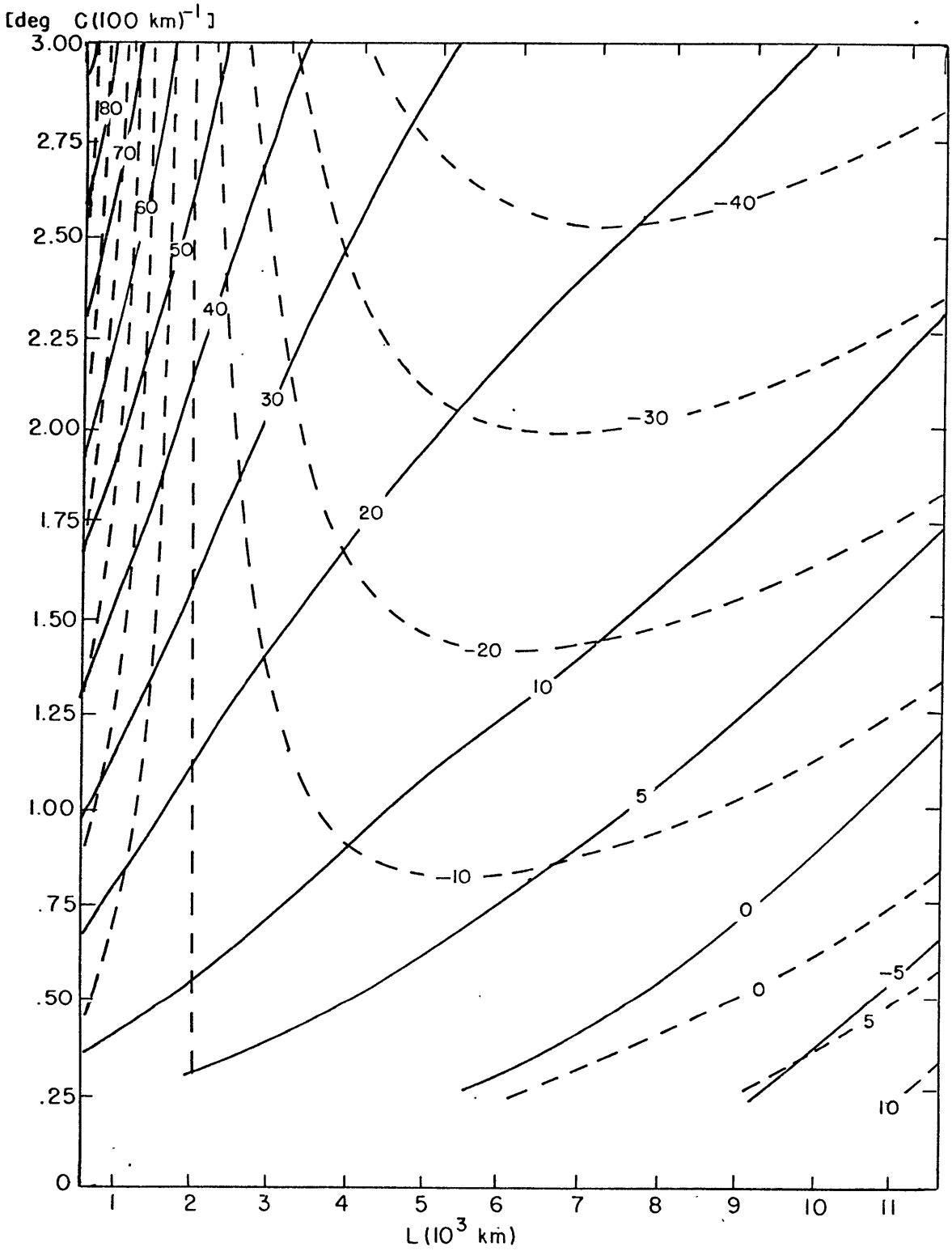

Fig. 7b. Part b indicates the same parameters except for η_o/T $\gamma = 11.2 \times 10^{-6}$ sec^{-1} $^oC^{-1}$.

of figure 7 may be compared directly with figure 16 of Sanders' work (1971). We see that, although the overtaking rates are much higher in this model for certain high a values and small wavelengths, that an overtaking rate of about 5 m/sec is indicated for the wavelengths of maximum deepening (see figure 2). This is quite similar to the results found in the earlier model. A look at part B of figure 7 shows for this larger vorticity-stability value that for the maximum deepening wavelengths, the overtaking rate for a large number of a values is only about 2 - 3 m/sec. The fact that significant deepening of the storm can occur without the tendency to occlude (see figures 2 and 7), along with the trend of the less overtaking by the 250 mb trough with increasing values of vorticity-stability, points to the likelihood that some other process cuts off the storm intensification. A sampling of rapidly deepening storms found in a synoptic lab class at M.I.T. showed no clear trend to occlude. Thus, friction, which has yet to be considered, might be expected to cut off the deepening of a storm, rather than the process of occlusion.

IIe. Temperature Perturbation Tendency

Now, we wish to consider the rate of intensification (or lack of it) of the temperature perturbation. The tendency of the thickness of the 1000 - 250 mb layer at the cold trough (x = 0, y = 0) is

$$\mathfrak{T}(0,0,250\,\text{mb}) - \mathfrak{T}(0,0,p_0) = \left[\hat{\mathfrak{T}}_2(250) - \hat{\mathfrak{T}}_2(p_0)\right] \sin\frac{2\pi}{L}x \tag{35}$$

From our expression for $\hat{\mathfrak{T}}_2$, we have

$$\left[\hat{\mathfrak{T}}_2(250) - \hat{\mathfrak{T}}_2(p_0)\right] = \left(\frac{2\pi}{L}\right)\frac{\hat{p}_{10} R_d \ln 4}{f_0} + \frac{\lambda_0 \hat{p}_{10} q}{\left(\frac{2\pi}{L}\right) f \Gamma_0}\left[\frac{p_T q_1\left[\left(\frac{1}{4}\right)^{(q_1-1)} - 1\right] - p_0 q_1\left[1 - (4)^{(q_1-1)}\right] + p_0(1-q_1)\left[1 - \left(\frac{1}{4}\right)^{q_1}\right] - p_T(1-q_1)\left[(4)^{q_1} - 1\right]}{\left(p_T q_1 p_0^{(1-q_1)} - p_T^{(1-q_1)} p_0 q_1\right)}\right] \tag{36}$$

Equation (36) indicates a different wavelength dependence in each of the two terms on the right side, so that a critical wavelength is indicated, below which no intensification will occur. Because this dependence appears similar to the expression in Sanders' equation 40 (1971), we should expect a similar pattern of thickness tendency in our calculations to those of Sanders' version. Figure 8 shows these patterns, but we also see a major improvement over the earlier formulation. That is, for each vorticity-stability value and for ($0 < \lambda < 4/4$), the wavelength of maximum deepening is also a wavelength at which the temperature perturbation is intensifying. The opposite situation exists in

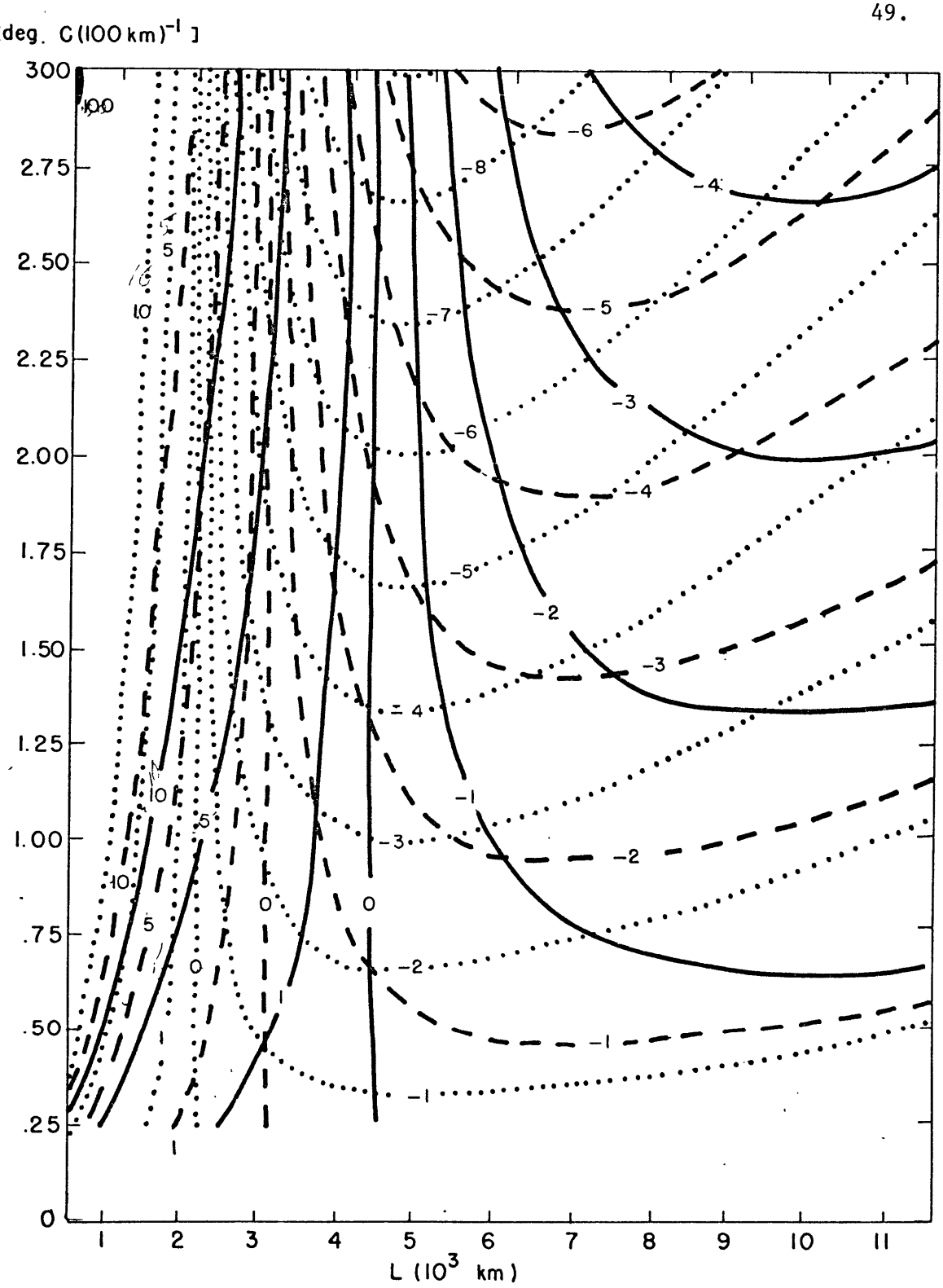

Fig. 8a. The difference $\hat{\chi}_2$ at 250mb and $\hat{\chi}_2$ at 1000mb, for λ = L/4 as a function of wavelength and meridional temperature gradient for the same selection of vorticity-stability values as explained in figure 2. The isopleth units are in $10^{-2}m^2sec^{-2}$. The mean temperature tendency in the troposphere is indicated by this difference.

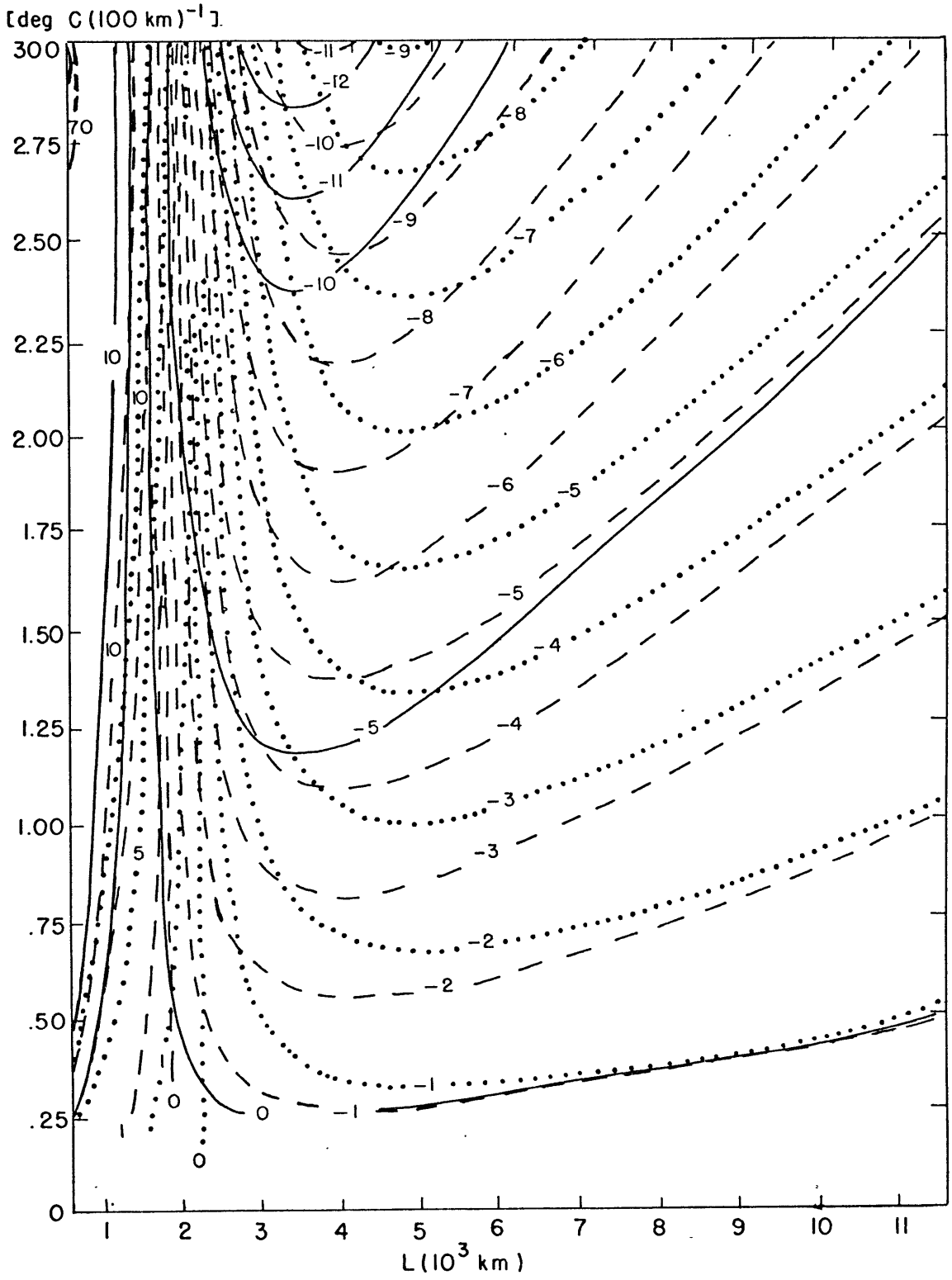

Fig. 8b. Same as for 5a, except for vorticity-stability values of 5.6, 8.4, and 11.2 sec^{-1} ^{o}K^{-1} .

the first version of the model. By examining figures 2 and 8, we see that for $a = 2.0 \times 10^{-5}$°C m^{-1} and $\lambda_0/\tau_0\gamma = 2.8 \times 10^{-6}$ sec^{-1}°K^{-1}, the temperature perturbations are intensifying at around 2.0 °C/12 hours for the preferred wavelength of deepening. As the vorticity-stability parameter increases, there appears to be a tendency for this intensification rate to increase for the wavelength of maximum deepening. Thus, with this version of the model, which tends to be especially realistic for maritime cases, the intensification of the storm actually occurs simultaneously with the intensification of the temperature perturbation. That is, zonal available potential energy is converted to eddy available potential energy in this model, as deepening occurs.

IIf. Frictional Effects

A calculation of the filling rate of a storm due to friction necessitates an understanding of what the frictional force is at the ground, and also how it acts above the surface. Rather than specifying a cross-isobaric flow and a lower boundary value of (due to friction) at the top of the surface friction layer (see, for example, Sanders, 1971), we shall make an attempt to find an analytic solution to the equation with frictional forcing

$$\left(\nabla^2 + \frac{f_0 \lambda_0}{\sigma} \frac{\partial^2}{\partial p^2}\right) \omega_\psi = -\frac{f_0}{\sigma} \frac{\partial}{\partial p}\left(\underset{\sim}{k} \cdot \nabla \times \underset{\sim}{f}\right) \tag{37}$$

where ω_ψ is the vertical motion due to frictional convergence or divergence, and $\underset{\sim}{f}$ is the frictional force vector per unit mass. The solution to (37) depends, of course, on how we specify $\underset{\sim}{f}$; and if we define $\underset{\sim}{f}$ to be linearly proportional to the 1000 mb geostrophic velocity vector, analytic solutions may be found. Haltiner (1971) finds the vertical motion at the top of the boundary layer using both a linear relationship, and a (velocity)^2 dependence. Of course, the latter dependence would be preferable, but solving the ω-equation would become much less manageable. If we further assume that the frictional force acts in an opposite direction from this wind vector, then

$$\underset{\sim}{f} = -\epsilon(p)\, \underset{\sim}{V}_{1000} \tag{38}$$

Now, equation (37) becomes

$$\left(\nabla^2 + \frac{f^2 N_0}{\sigma}\frac{\partial^2}{\partial p^2}\right)\omega_\psi = \frac{f_0}{\sigma}\zeta_{1000}\frac{\partial \epsilon}{\partial p}$$

Further, it is physically reasonable to parameterize the frictional force such that it is a maximum at the ground, and damps off exponentially with height, so that it becomes $(1/e)$ times its 1000 mb value at the top of the surface boundary layer (say, at 900 mb) and vanishes at $p = 0$. Thus,

$$\epsilon(p) = \frac{C_d V_0}{\Delta z}\left(\frac{e^{\left(\frac{p}{p_0}\right)^2} - 1}{e - 1}\right) \tag{39}$$

where C_d is the surface drag coefficient, V_0 is a specified value of the 1000 mb wind (independent of horizontal position), and Δz is the depth of the boundary layer (usually about 1 km and corresponding to the pressure scale height of 900 mb). Thus, at 1000 mb, the frictional force per unit mass is

$$\underset{\sim}{F} = \frac{-C_d V_0}{\Delta z}\underset{\sim}{V}_{1000}$$

We see that $\underset{\sim}{F}$ is proportional to the square of the velocity, at least superficially. The limitations here are that $\underset{\sim}{V}_{1000}$ will be a rather large overestimate of the 1000 mb wind in a cyclone, while V_0 is a constant value defined for the region at 1000 mb under the influence of frictional convergence of divergence. Although the specified value of V_0 appears to be the most serious limitation of our formulation, somewhat less ad-hoc decisions must be made for the values of C_d, Δz, and $\hat{\phi}_{10}$.

Mindful of these foregoing liabilities, we shall proceed now with the business of finding a solution to (37). The 1000 mb vorticity may be expressed geostrophically as $\zeta_{10} = \nabla^2 \phi_{10}/f_0$, where, as before

$$\phi(X,Y,p_0) = \hat{\phi}_0 \cos\frac{2\pi}{L}(X+\lambda)\cos\frac{2\pi}{L}Y$$

so that

$$\nabla^2\phi_{10} = -2\left(\frac{2\pi}{L}\right)^2\hat{\phi}_{10}\cos\frac{2\pi}{L}(X+\lambda)\cos\frac{2\pi}{L}Y$$

Now, equation (37) becomes

$$\left(\nabla^2 + \frac{f_0^2\nu_0}{\sigma}\frac{\partial}{\partial p^2}\right)\omega_4 = -\frac{2}{\sigma}\left(\frac{2\pi}{L}\right)^2\hat{\phi}_0\frac{\partial\zeta}{\partial p}\cos\frac{2\pi}{L}(X+\lambda)\cos\frac{2\pi}{L}Y \qquad (40)$$

If we assume that ω_4 has the same horizontal structure as its forcing, set the boundary conditions as $\omega_4 = 0$ at $p = p_o$ and $p = 0$, solve analytically for the homogeneous solution, and approximate the particular solution by a Taylor's series, then the solution to (40) is

$$\omega_4 = \left\{\frac{-k_4 p_0^8\left(\frac{p}{p_0}\right)^{q_{11}}}{a_1}\left[\frac{1}{(8-q_{11})(8-q_{12})} + \frac{1}{(15-q_{11})(15-q_{12})} + \frac{1}{2!(22-q_{11})(22-q_{12})}\right]\right.$$

$$\left. + \frac{k_4 p^8}{a_1}\left[\frac{1}{(8-q_{11})(8-q_{12})} + \frac{p^7}{p_0^7(15-q_{11})(15-q_{12})} + \frac{p^{14}}{p_0^{14}2!(22-q_{11})(22-q_{12})}\right]\right\}$$

$$\times\left[\cos\frac{2\pi}{L}(X+\lambda)\cos\left(\frac{2\pi}{L}Y\right)\right] \qquad (41)$$

where

$$k_\psi = \frac{-4\psi}{p_0^2}\left(\frac{2\pi}{L}\right)^2 \frac{\hat{\phi}_{10}\, C_d V_0}{RT_0 \gamma\, \Delta z\,(\sigma-1)}$$

$$q_{11} = \frac{1}{2} + \frac{1}{2}\sqrt{1+4\left(\frac{b_1}{a_1}\right)}$$

and

$$q_{12} = \frac{1}{2} - \frac{1}{2}\sqrt{1+4\left(\frac{b_1}{a_1}\right)}$$

The reader might reasonably ask why we did not set the upper boundary condition of $\omega_\psi = 0$ at $p = p_T$, as was done with the other components of ω. The answer is that the frictional forcing is parameterized to be small enough at higher levels, so that ω is virtually negligible at the tropopause level anyway. This fact is quantitatively shown in figure 9, where a vertical profile of ω_ψ over the surface low is shown for the parameter of our sample case C. A drag coefficient of 2.0×10^{-3} (a typical land value, see Cressman, 1960), $V_o = 10$ m/sec, and $\Delta z = 1$ km were used in the computations. We see that the maximum value of ω_ψ is found at about 850 mb, with an exponential-like decrease above this level. The values are somewhat less than the largest components of vertical motion found in figure 1, but still will be important when we consider the effect of convergence and divergence in the height tendency. The ω-profile shown in figure 9 shows what we would qualitatively expect from quasi-geostrophic theory with the convergence confined to the lower troposphere and the divergence above (in this case, 850 mb).

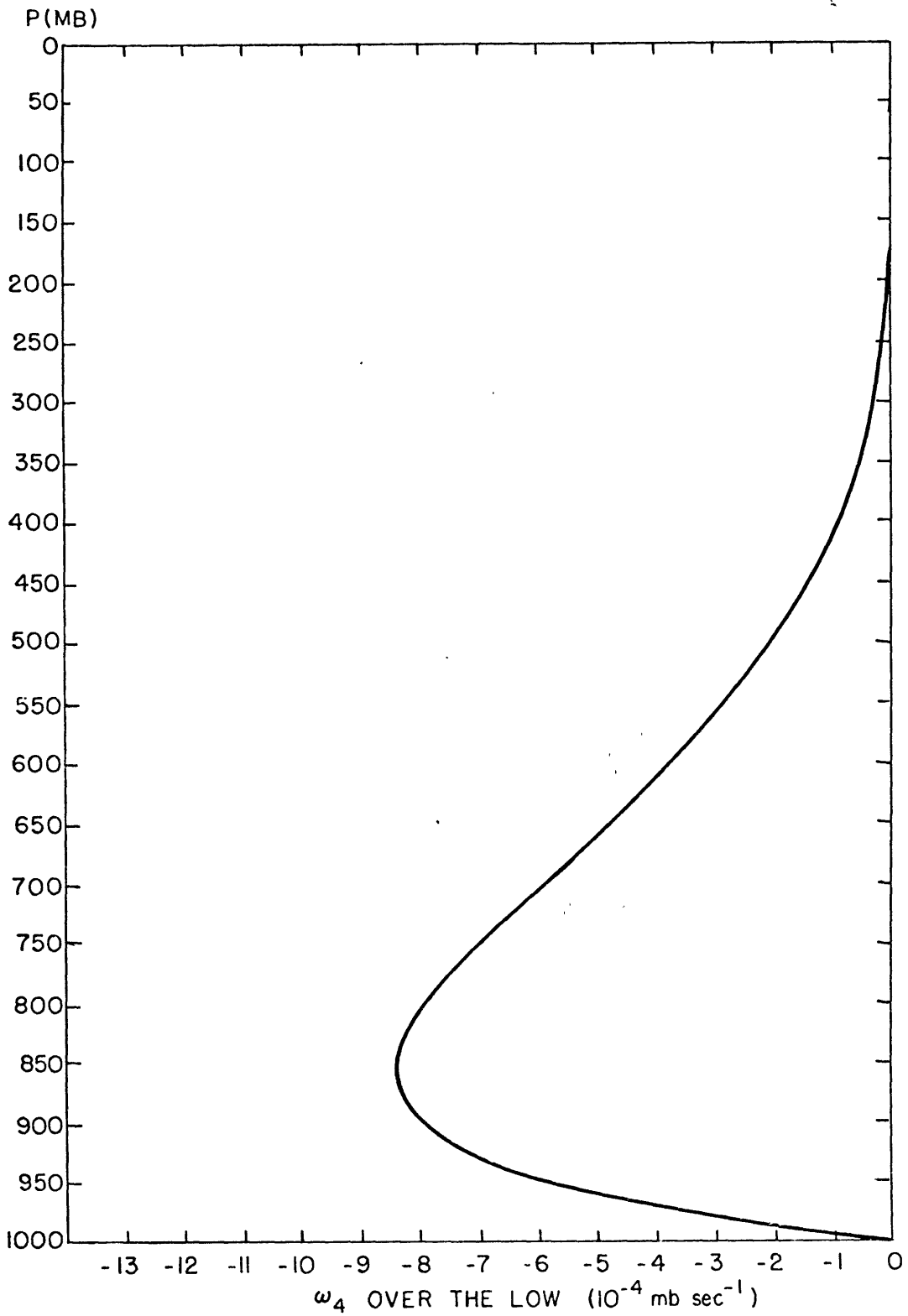

Fig. 9. The frictional vertical velocity over the 1000mb center with units in 10^{-4}mb sec^{-1} , case C.

The 1000 mb height should be rising, because the larger dissipative effect of friction exceeds the tendency of the convergence in the lower layers to cause the heights to fall. We need to look at the height tendency equation to verify this fact.

The χ -equation due to the forcing by frictional dissipation and divergence may be expressed as

$$\nabla^2 \chi_4 = f_0 \eta_0 \frac{\partial \omega_4}{\partial p} + f_0 \vec{k} \cdot \nabla \times \vec{F} \tag{42}$$

where χ_4 is the height tendency due to the frictional effects on the right side of (42). If we regard χ_4 as having the same x and y dependence as its forcing functions, then

$$\chi_4 = \hat{\chi}_4 \cos\frac{2\pi}{L}(x+\lambda)\cos\frac{2\pi}{L}y \tag{43}$$

where

$$\hat{\chi}_4 = \frac{-7\hat{\phi}_{10}}{(\sigma-1)}\left(\frac{c_d V_0}{\Delta z}\right) q_{11}\left(\frac{p}{p_0}\right)^{(q_{11}-1)}\left[\frac{1}{(8-q_{11})(8-q_{12})} + \frac{1}{(15-q_{11})(15-q_{12})} + \frac{1}{2!(22-q_{11})(22-q_{12})}\right]$$

$$+\frac{7\hat{\phi}_{10}}{(\sigma-1)}\left(\frac{c_d V_0}{\Delta z}\right)\left(\frac{p}{p_0}\right)^7\left[\frac{8}{(8-q_{11})(8-q_{12})} + \frac{15\,p^7}{p_0^7(15-q_{11})(15-q_{12})} + \frac{22\,p^{14}}{p_0^{14}\,2!(22-q_{11})(22-q_{12})}\right]$$

$$-\frac{\hat{\phi}_{10} c_d V_0\left(e^{\left(\frac{p}{p_0}\right)^7}-1\right)}{\Delta z(e-1)}$$

The last term above represents the effects of frictional dissipation, while the other terms are the result of the divergence of ω_4 . At the low

center, $x = 4/2 - \lambda$, $y = 0$, and the signs of each of the terms in the $\hat{\mathcal{J}}_4$ expression are reversed so that we can see physically that the dissipation term represents a height rise, as expected. Using the same numbers as above for C_d , V_6 , and δz , we find the $\mathcal{J}_4$ value over the low for case C at 1000 mb is 61 x 10^{-4} m^2/sec^3, which corresponds to a filling rate of +3.6 mb/12 hours. This, when combined with our frictionless deepening of the case C storm (-12.0 mb/12 hours), yields a net intensification of -8.4 mb/12 hours - quite close to the observed rate of -8 mb/12 hours. Our computed value of ($\mathcal{J}_1 + \mathcal{J}_4$) is much closer to the observed number than the figure found in the original model version. Whether this is due to a better formulation for $\hat{\mathcal{J}}_1$, or $\hat{\mathcal{J}}_4$ is not clear; the magnitudes of both numbers are larger in this model, and it is exceedingly difficult to successfully "observe" the frictional filling rate in the real atmosphere.

The parameter q_{11} increases with decreasing wavelength with all the other input values being held constant. However, it is not immediately clear from (43) how $\hat{\mathcal{J}}_4$ behaves as L decreases. Indeed, as in the previous model, the filling rate does increase with decreasing L, providing for a shortwave cutoff, assuming $\hat{\phi}_{10} \neq 0$. We also have a limiting intensity established because $\hat{\mathcal{J}}_1$ is independent of $\hat{\phi}_{10}$, while $\hat{\mathcal{J}}_4$ is directly proportional to it. Using $\hat{\phi}_{10} = 1020\ m^2(sec)^{-2}$ for the sample case C, the limiting intensity $\hat{\phi}_{L10}$ may be expressed as

$$\hat{\phi}_{L10} = \frac{\hat{\mathcal{J}}_1}{\left(\frac{\hat{\mathcal{J}}_4}{1020.}\right)}$$

For our sample case C, this value is 3.43×10^3 m^2 sec^{-2}. The range of sea-level pressures that this value corresponds to is about 93 mb. This increased value over the earlier results is due to generally greater increased values of $\hat{\zeta}_1$ than $\hat{\zeta}_4$.

III. Experiments with the Frictional Expression

As a check on the reliability of the aforementioned frictional formulation, we examined some cases of rapidly deepening cyclones over the North American continent, where surface analyses indicating the deepening rates and evolution of the cyclone structure are more reliable than over the sea. The 1000 - 250 mb thickness analysis is presumably accurate in land areas, where upper air observations are sufficiently dense to achieve this accuracy. Specifically, an experiment was undertaken to check on whether our frictional formulation is sufficient to account for the observed thickness change over the center.

Reference is made to the discussion given by Sanders (1976). The quasi-geostrophic vorticity equation for flow at sea-level is

$$\frac{\partial \zeta_{SL}}{\partial t} = \underset{\sim}{V}_{SL} \cdot \nabla \left(\zeta_{SL} + f\right) + \eta_0 \left(\frac{\partial \omega}{\partial p}\right)_{SL} + \underset{\sim}{k} \cdot \nabla \times \underset{\sim}{F}$$

where the subscript SL refers to sea-level, η_0 is a constant value of absolute vorticity for the appropriate domain, and $\underset{\sim}{F}$ is the frictional force per unit mass as previously defined. The advection term disappears at the center of the cyclone. The relative vorticity is given as

$$\zeta_{SL} = \frac{1}{\rho_{SL} f_0} \left(\nabla^2 p_{SL}\right)$$

where ρ_{SL} and f_0 are both regarded as constant values of the sea-level density and the Coriolis force. The harmonic variation of p_{SL} with respect to x and y yields

$$\eta_{sL} = -\left(\frac{2\pi}{L}\right)^2 \frac{\hat{p}_{sL}}{\rho_{sL}(f_o)}$$

where $\hat{p}_{sL}$ is the semi-amplitude of p_{sL}, and L is its wavelength. Now, our vorticity equation becomes an expression for the central pressure tendency, $\partial \hat{p}_{sL}/\partial t$, and by assuming a linear structure of with height from a zero value at 1000 mb to its maximum at 600 mb, we have

$$\frac{\partial \hat{p}_{sL}}{\partial t} = \rho_{sL} f_o \eta_o \frac{L^2}{(2\pi)^2}\left(\frac{w_s}{400\ mb.}\right) - \epsilon(sL)\hat{p}_{sL} \qquad (44)$$

This latter assumption may not be too accurate if the storm is quite intense, and the components of the frictionally induced vertical motion becomes larger, resulting in a maximum w below 600 mb. Thus, in this, the sea-level divergence would be assumed to be larger by decreasing the denominator above (the pressure difference through which w increases to its maximum).

Defining $\epsilon(sL) = \frac{C_d V_o}{\Delta z}$, we will use V_o as a typical domain averaged value of the sea-level wind velocity, and use the same numerical value as before: $C_d = 2.0 \times 10^{-2}$, $V_o = 10$ m/sec, and $\Delta z = 1000$ m. The equation for the local rate of change of thickness (in the 1000 - 500 mb layer) $\partial h/\partial t$, ignoring diabatic effects and differences in the surface boundary layer (where w is small, anyway), may be expressed, according to Sanders (1976) as

$$\frac{\partial h}{\partial t} = \frac{R}{g}\left(\frac{\omega_6}{2}\right)\left(\overline{\frac{T}{\theta}}\right)\left(\frac{\theta_5 - \theta_{8.5}}{350\ mb.}\right)\ln 2 \qquad (45)$$

Equation (45) represents adiabatic effects due to vertical motion on the thickness change, ($\left(\overline{\frac{T}{\theta}}\right)$) indicates the average of this value in the layer and will be taken as a constant value .92 . Now, we proceed to eliminate ω_6 between equations (44) and (45), by expressing ρ_{SL} in terms of P_{SL} and T_{SL} from the ideal gas law, and assigning typical values to the following parameters: $f_o = \gamma_o = 10^{-4}$ sec^{-1}, T_{SL} = 273°K, P_{SL} = 1000 mb. Thus, expressing L in thousands of km, we have

$$\frac{\partial h(m.)}{\partial t} = 3.28\frac{(\theta_5 - \theta_{8.5})}{L^2}\frac{\partial \hat{P}_{SL}(mb.)}{\partial t} + 3.28\frac{(\theta_5 - \theta_{8.5})}{L^2}\epsilon_{SL}\hat{P}_{SL}(mb.) \qquad (46)$$

If the layer under consideration is saturated, then we should take into account latent heat release by expressing the stability in terms of the moist adiabatic lapse rate. Thus $(\theta_5 - \theta_{8.5})$ would be replaced by $[(\theta_5 - \theta_{8.5}) - (\theta_5 - \theta_{8.5})_{md}]$. So, in this case, we have

$$\frac{\partial h(m.)}{\partial t} = \frac{3.28\left[(\theta_5 - \theta_{8.5}) - (\theta_5 - \theta_{8.5})_{md}\right]}{L^2}\frac{\partial \hat{P}_{SL}(mb.)}{\partial t} + \frac{3.28\left[(\theta_5 - \theta_{8.5}) - (\theta_5 - \theta_{8.5})_{md}\right]}{L^2}\epsilon(SL)\hat{P}_{SL}(mb.) \qquad (47)$$

Equation (47) shows that the static stability is effectively reduced for the moist case. The physical significance of both equations (46) and (47) is that convergence at the surface, which increases the vorticity and causes central pressure falls, also adiabatically cools the layer above through upward motion, when the atmosphere is stable. There is an additional frictional effect, which implies that the thickness decreases locally with cyclonic vorticity due to frictional covergence and the resulting upward motion.

The first and second terms of (46) and (47) were isolated and evaluated for the various cases to determine $\partial h/\partial t$. However, we must also take into account the movement of the storm toward warmer or colder air. Thus, if the storm is moving with a velocity vector $\underset{\sim}{C}$, the local thickness change following the center $\left(\partial h/\partial t\right)'$ may be expressed as

$$\left(\frac{\partial h}{\partial t}\right)' = \underset{\sim}{C}\cdot\nabla h + \frac{\partial h}{\partial t} \qquad (48)$$

Generally, the surface cyclone moves to the right of the upper level flow and thus toward warmer air (see Sanders, 1971). So the local change of thickness over the center is usually due to the opposing effects of movement to higher thickness values and cooling due to adiabatic ascent.

A balance in equation (48) is sought in the sampling of land cases, using the frictional term in (46) or (47). First, however, we should make this procedure more applicable to the standard 12-hour time interval. found between map times. A similar procedure is discussed in Sanders (1976). From equations (48) and (46) or (47), depending upon whether we wish to use a dry or moist process, we integrate (48) over a twelve hour period and

find that

$$\Delta h = (\Delta h)' - \int_{t_0}^{t_0+12\,hr.} (\underset{\sim}{C}\cdot\nabla h)\,dt = k(\Delta \hat{p}_{SL}) + k\,\varepsilon_{SL}\,\hat{p}_{SL}(\Delta t)$$

where

$$k = \frac{3.28\left[(\theta_5-\theta_{8.5}) - (\theta_5-\theta_{8.5})_{md}\right]}{L^2}$$

for moist processes, and

$$k = \frac{3.28(\theta_5-\theta_{8.5})}{L^2}$$

for dry (unsaturated) air, where Δh is the local 12-hour thickness change over the cyclone center in a coordinate system fixed on the earth's surface (which can be obtained from the 12-hour change of the central pressure and from an appropriate static stability value), and $(\Delta h)'$ is the 12-hour thickness change following the center in a coordinate system moving with the center, which is what we would like to determine. The integrated value of $\underset{\sim}{C}\cdot\nabla h$ over the 12-hour period may be approximately expressed as $\underset{\sim}{C}\cdot\nabla h = C\Delta h/\Delta s$, where Δs is the length of the 12-hour displacement vector with a speed C. Thus,

$$\int_{t_i}^{t_f} \underset{\sim}{C}\cdot\nabla h\,dt = \frac{\overline{\Delta h}}{\Delta s}\,C\cdot(12\,hr) = \overline{\Delta h}$$

where t_i and t_f are the times at the beginning and end of the 12-hour period, respectively. Now, we can approximate $\overline{\Delta h}$ by taking the average of the thickness differences between the upstream and downstream ends of the displacement vector for the cyclone, at the beginning and end of the twelve-hour period. Thus

$$\Delta h \approx \frac{1}{2}\left[\left(h_{id}-h_{iu}\right)+\left(h_{fd}-h_{fu}\right)\right] \approx \frac{1}{2}\left(h_{id}-h_{fu}\right)+\frac{1}{2}(\Delta h)' \tag{49}$$

so that now equation (48) becomes

$$(\Delta h)'-\left(h_{id}-h_{fu}\right)=2\Delta h=2k\Delta\hat{p}_{sL}+2k\left(\xi_{sL}\right)\hat{p}_{sL}\left(12hr.\right) \tag{50}$$

As has been pointed out by Sanders (1976), since we need know only the thickness values at the (id) and (fu) points, any errors in the thickness values near the low center will not contaminate the thickness analysis significantly at these latter mentioned points. In practice, the analyst would know from the surface and upper level analysis 12-hour earlier, h_{iu}, h_{id}, and $\hat{p}_{sL_i}$. These current analyses would indicate $\hat{p}_{sL_f}$ and h_{fu}. Now, taking $\Delta\hat{p}_{sL} = \hat{p}_{sL_f} - \hat{p}_{sL_i}$, $\hat{p}_{sL} = \frac{\hat{p}_{sL_i}+\hat{p}_{sL_f}}{2}$, $(\Delta h)' = h_{fd} - h_{iu}$, appropriate value of the static stability, and using the appropriate values of c_d, V_o, and Δz, we can estimate a value of (Δh)', and therefore of h_{fd}, the desired value of thickness over the low center at the current time. This procedure has been formulated for oceanic areas where there is likely to be a problem in knowing the value of the thickness, over the center, due to the likely small number of aircraft observations and satellite soundings, which will disclose only the large scale upper level patterns. Thus, if a ship's observations disclose the presence of a small intense cyclone near the surface, a likely overestimate of the thickness over the low center will result.

Using the procedure described above, we did some calculations of $(\Delta h)'$ for rather intense cases over land, where the thickness analysis is likely to be fairly reliable. Thus, we have somewhat of a check on our procedure before we attempt to use it over oceanic areas. These cases were chosen in mainly the north central part of the United States, where C_d values are likely to be around 2.0×10^{-3} (Cressman, 1960). Thus, C_d was evaluated at 2.0×10^{-3}, Δz = 1000 m, and V_0 = 10 m/sec for these cases. Four calculations were made for each of the time periods used in these cases: those of dry processes with and without friction and those of moist processes with and without friction. By "with and without friction", we mean including and not including the second term on the right-hand side of (50). The values of k, or equivalently, the static stability, were deduced from mean temperatures near the surface center at 850 and 500 mb. The numbers are summarized case by case in Table 1.

The time periods with an asterisk next to then indicate that the moist process was judged to be the relevant process taking place by virtue of the air being near saturation at both 850 and 500 mb. In the other cases, the air over the low was generally saturated at 850 mb, but at 500 mb, some drying out had taken place; so, unsaturated air was evident due to the dew point depression being at least 4^{o} K.

Thus, in the latter instance, we should expect that an observed thickness change over the center would be predicted by a value somewhere between our moist and dry with friction calculations. We see that for the moist cases, our moist with friction predictions are generally closer to the observed value than those predictions without friction. We note

Table 1

Calculated Thickness Changes over the Low Center

		dry processes		moist processes	
	$\Delta h'$ observed (m)	with friction (m)	without friction (m)	with friction (m)	without friction (m)
(Case of October 24-25, 1975)					
* 00Z, Oct. 25 - 12Z, Oct. 25	0	-133	+ 39	+ 28	+122
* 12Z, Oct. 25 - 00Z, Oct. 26	+ 60	- 70	+210	+130	+250
(Case of April 3-4, 1975)					
* 00Z, April 3 - 12Z, April 3	- 60	-475	- 22	-158	+100
* 12Z, April 3 - 00Z, April 4	0	-332	+ 38	-108	+100
(Case of March 3-5, 1974)					
00Z, March 4 - 12Z, March 4	-240	-400	- 18	- 36	+ 44
(Case of January 13-14, 1976)					
* 12Z, Jan. 13 - 00Z, Jan. 14	- 40	-224	- 58	- 46	+ 12
00Z, Jan. 14 - 12Z, Jan. 14	-110	-204	+ 28	- 60	+ 54

generally that since the low moves toward warmer air, the manner in which the air is cooled over the low is due to intensification and to frictionally induced upward motion.

On the basis of our results in Table 1, we feel that our frictional parameterization does a reasonably good job of helping to account for observed thickness changes over the low. Without this frictional effect, a calculation of thickness tendency would likely not cool the low sufficiently to correspond with the observed change.

IV. The Sounding Sample

In order to find typical values of potential temperature differences in the above expressions for intense oceanic cyclones, and also to look at the vertical structure of relative humidity, we collected a sample of radiosonde observations taken under the influence of strong maritime storms (with at least 12 mb/12 hour deepening at some point in its life history) over a period from 1971 to 1974 (Northern Hemisphere Data Tabulations). The observations were used at either the time before which the above mentioned deepening occurred or just after such a period. Aside from this temporal stratification, the domain of the observations was divided into four quadrants, separated by boundaries being defined by the lines along and normal to the path of the storm. The outer limit of the quadrant is defined by the crossover points for the change from cyclonic to anticyclonic curvature of the sea-level isobars. Just over seventy soundings have been collected for each time period. The spatial distribution of the sounding locations within a normalized square containing the four quadrants is shown in figure 10 for each time period.

Composite soundings are shown in figures 11 and 12 stratified by time, quadrant, and case. This latter separation is done only for the convenience of being able to discern individual plots. Solid lines indicate relative humidity $\geq$ 75% and dashed lines indicate values $<$ 75%. According to the quadrants presented in figure 11, the mean stability for before deepening cases ($\theta_5 - \theta_{8.5}$) is generally similar and about 22°K, except in the left rear quadrant where somewhat less stable air is present, mainly in lower levels, for a value of about 17°K. Values of $[(\theta_5 - \theta_{8.5}) - (\theta_5 - \theta_{8.5})_{mq}]$ for saturated air range

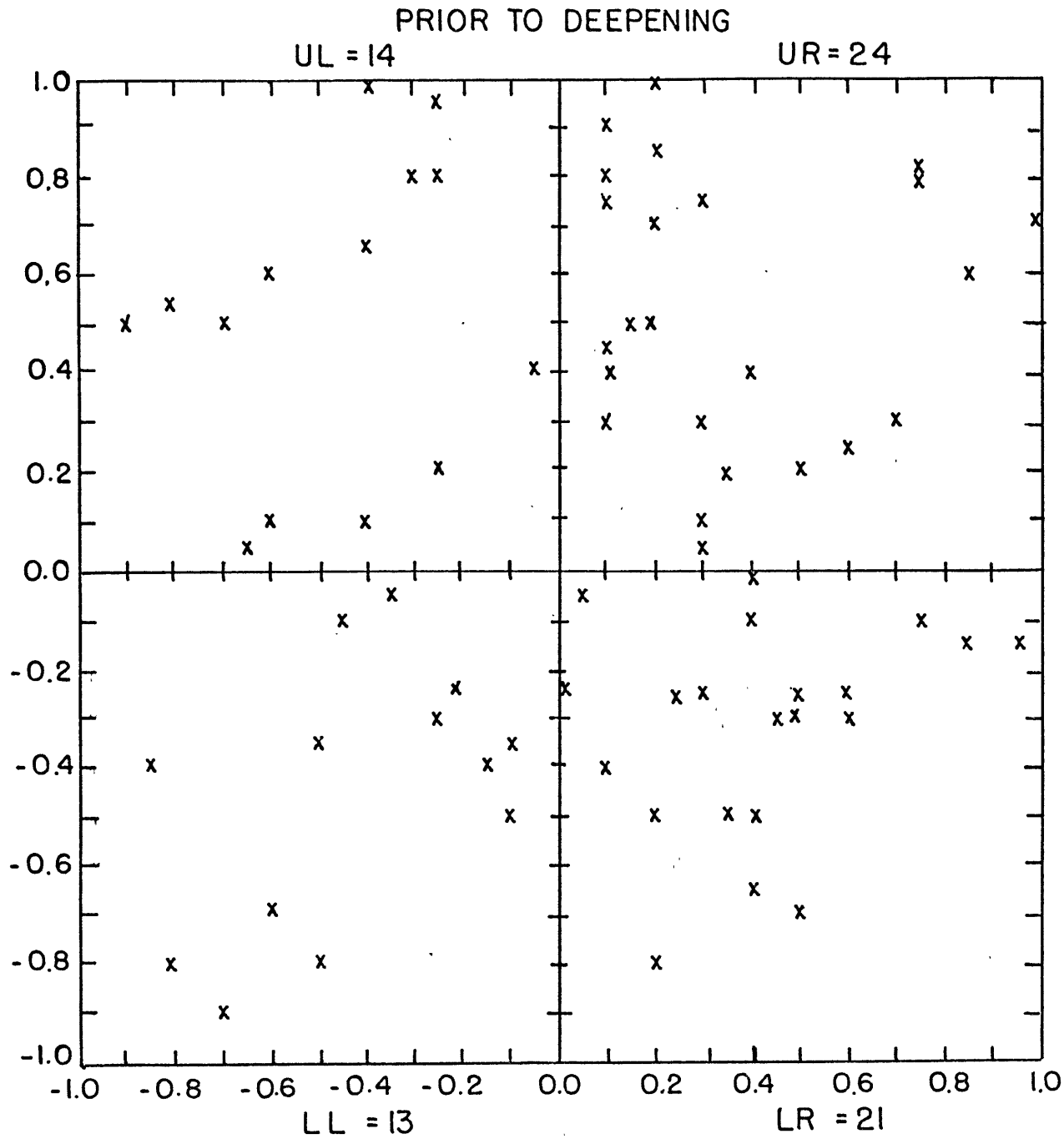

Fig. 10a. Normalized square containing the relative locations of the individual soundings for "before" deepening. The number of soundings in each quadrant is indicated. The motion of the low is from left to right.

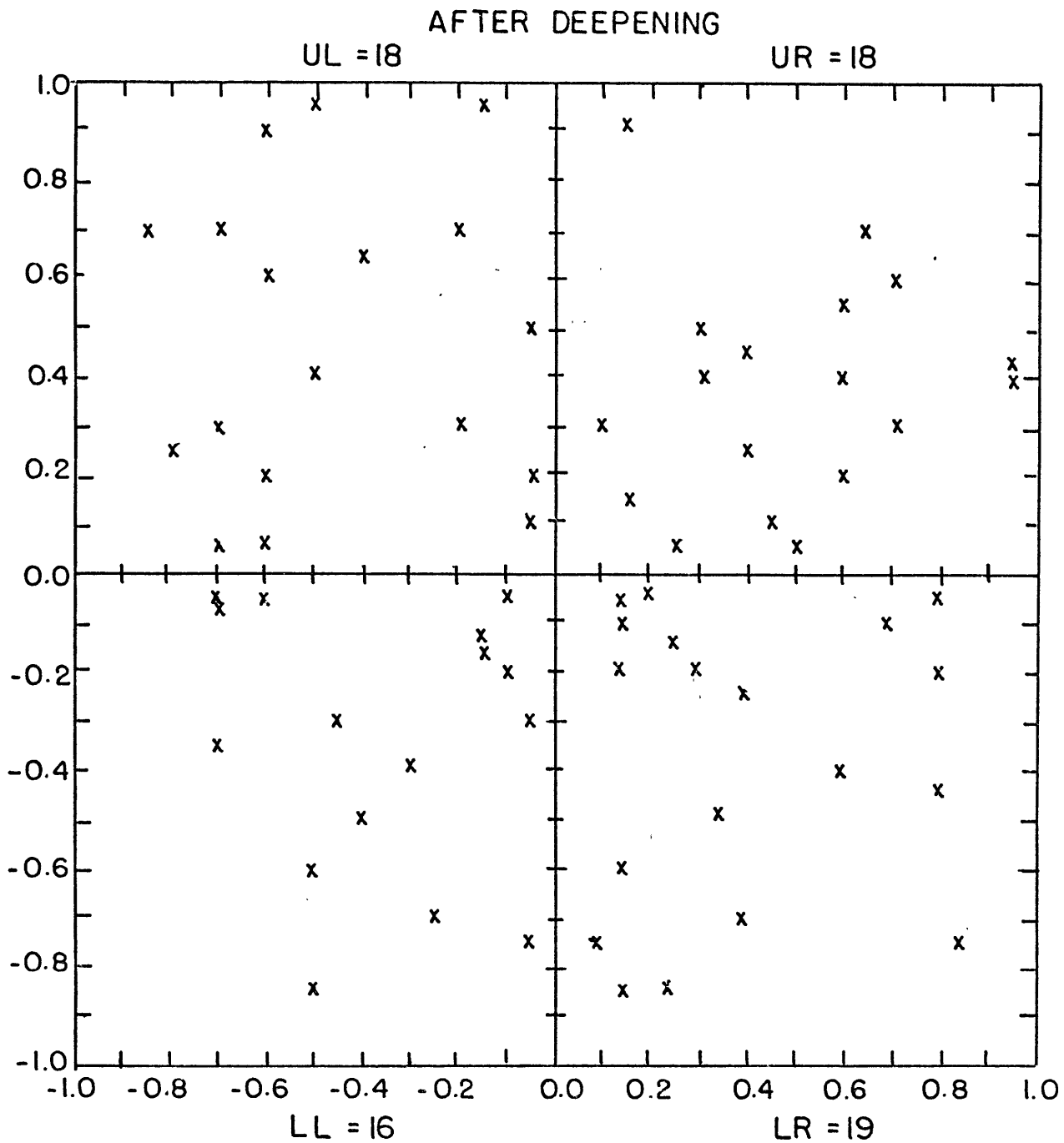

Fig. 10b. Same as for 10a except for the "after" deepening cases.

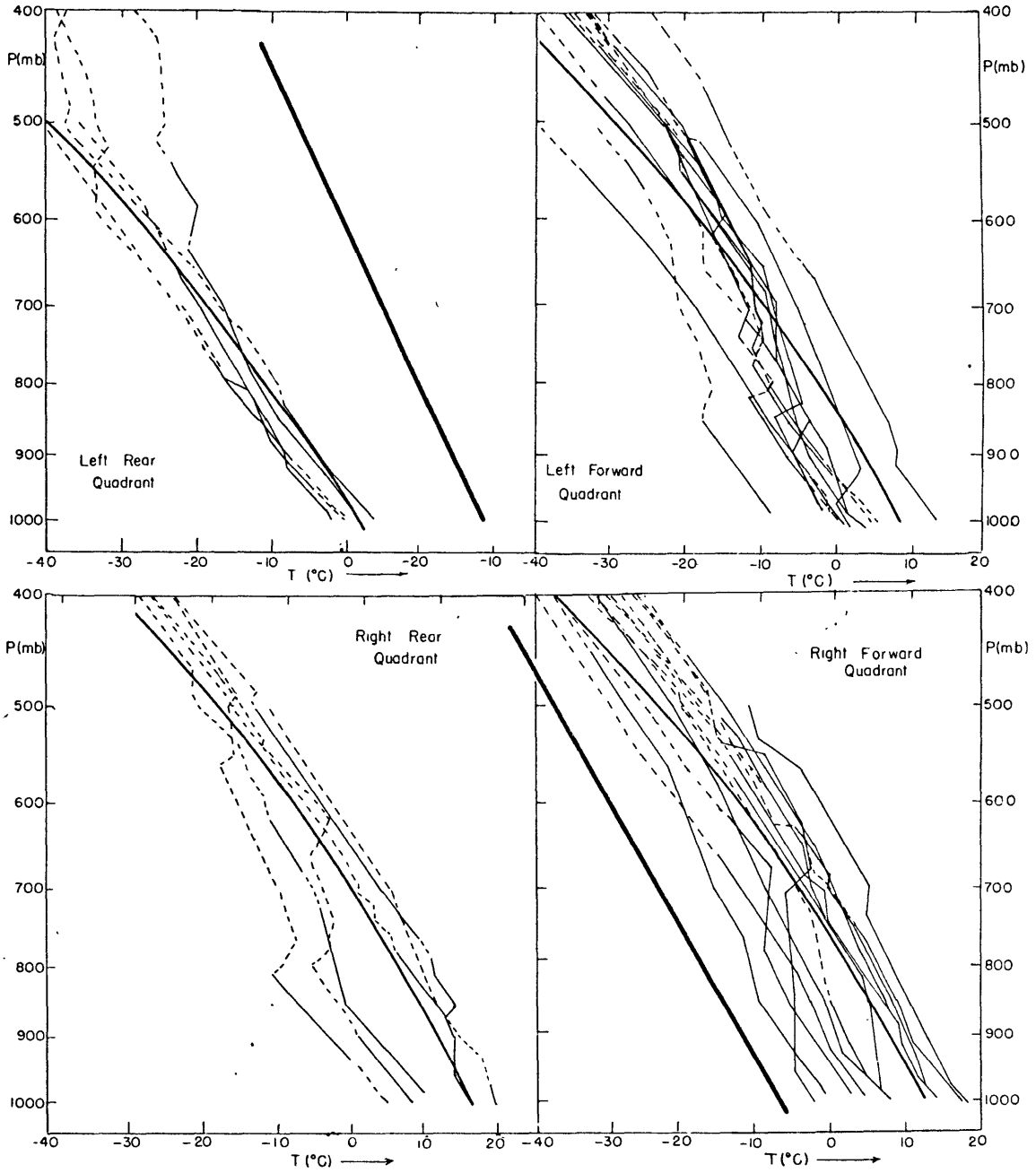

Fig. 11a. Composite soundings from areas under the influence of intense oceanic storms for the "before deepening" regimes. Solid lines indicate approximately levels at which the air has relative humidity $\geq$ 75%, simulating saturated conditions. Dashed lines are for unsaturated conditions.

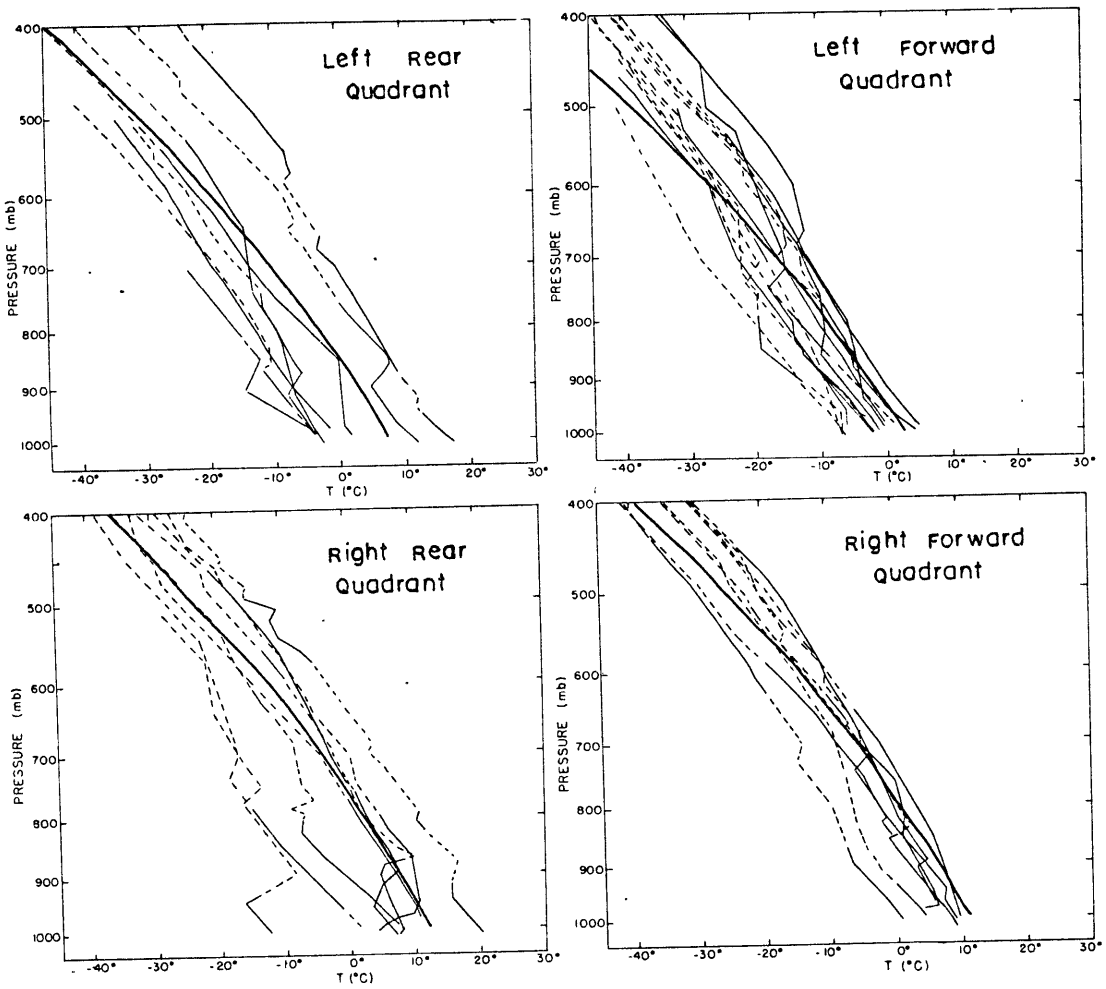

Fig. 11b. Part A is for cases 1 to 35
Part B is for cases 36 to 60

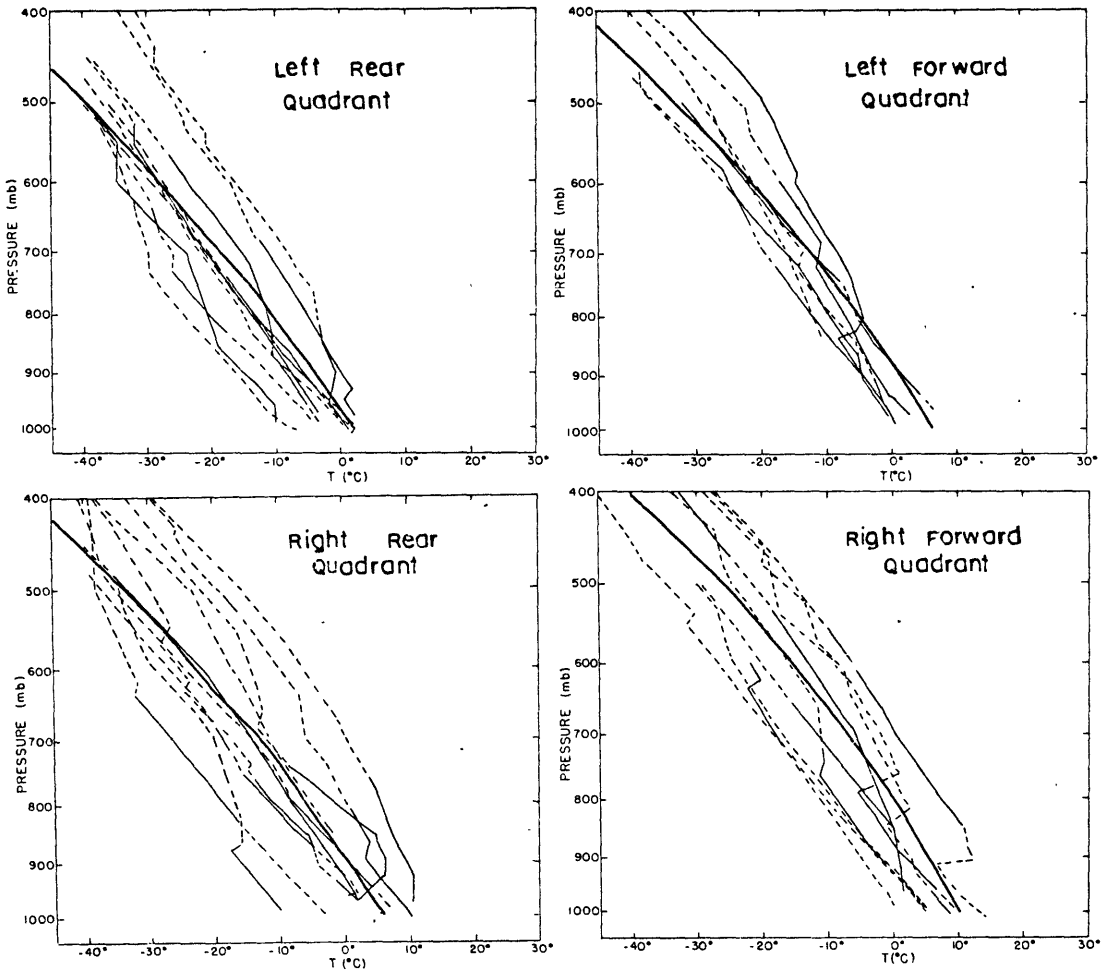

Fig. 12a. Same as for Fig. 11, except for "after deepening cases". Part A is for cases 1 to 40.
Part B is for cases 41 to 60.

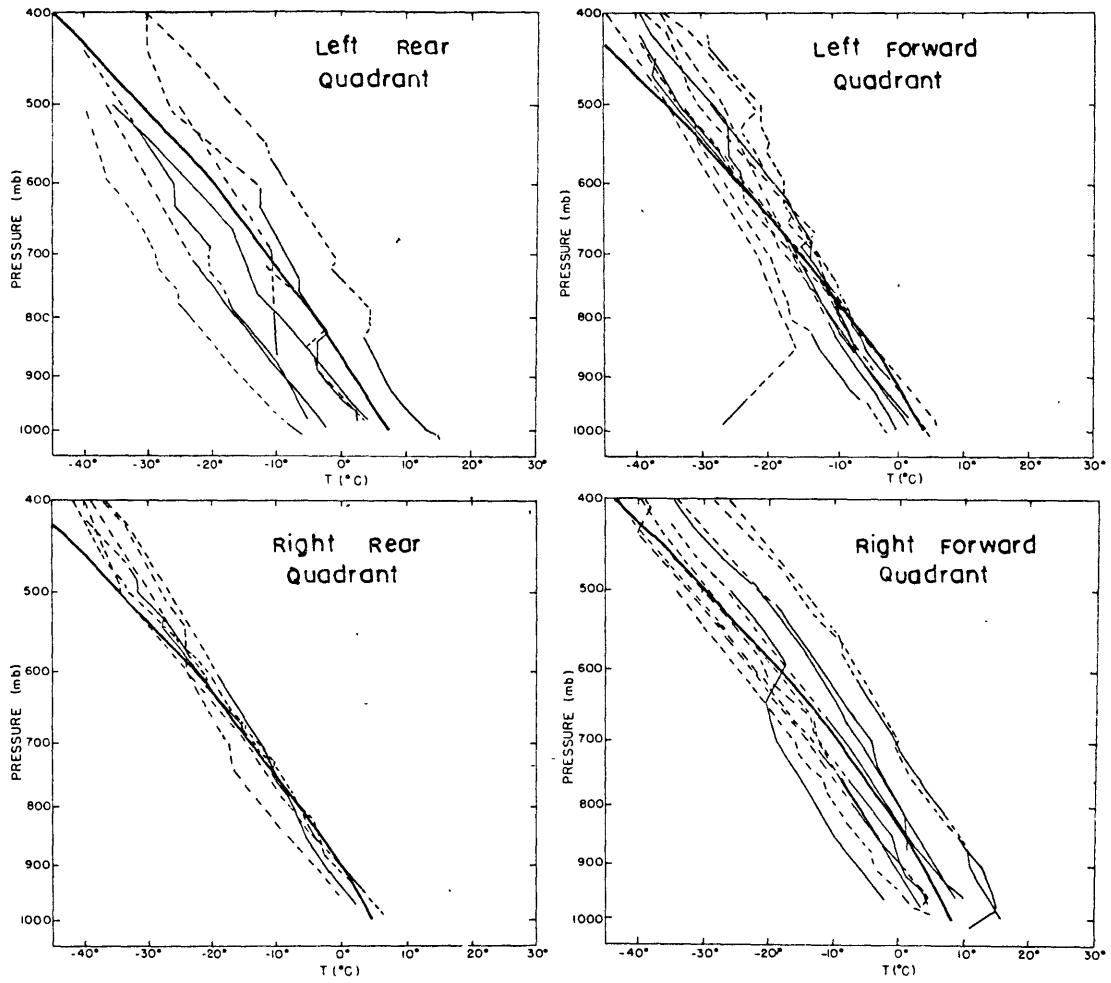
Left Rear Quadrant
Left Forward Quadrant
Right Rear Quadrant
Right Forward Quadrant
PRESSURE (mb)
T (°C)
400
500
600
700
800
900
1000
-40°
-30°
-20°
-10°
0°
10°
20°
30°

Fig. 12b.

from 7 - 10°K in all the quadrants except the left forward, where the stability value is higher at 13°K. The mean stability values, averaged over all the quadrants are about 20°K and 10°K, for dry and moist processes, respectively. Values of the factor, K, in either equation (46) or (47)

$$\frac{\partial h}{\partial t} = K\left(m./mb.\right)\left(\frac{\partial \hat{p}_{sc}}{\partial t} + \epsilon(sc)\hat{p}_{sc}\right)$$

are found in Table 2 for both prior and after deepening cases.

The values of K are included for the after deepening cases to show any possible differences in stability between the two time periods.

These differences are more easily seen in figure 13, which shows the mean vertical structure of temperature and relative humidity for each quadrant and time period. We are almost immediately struck with the fact that the stability in all quadrants, except for the left rear, decreased from the time before maximum deepening to the time after this deepening occurred. The stability (based on the 850 - 500 mb layer) in the left rear quadrant remained the same for this sampling of cases. We are most confident on the basis of traditional sampling theory (the student t-test) of the stability changes in the two forward quadrants. We can only speculate here as to the possible causes of this apparent destabilization. A warming trend is found in the left forward quadrant at 850 mb during the life of the cyclone, while an average drop of 1.0°C. takes place at 500 mb. The right forward quadrant, where we are the most confident of a stability decrease, shows cooling at both levels, with a greater temperature decrease at 500 mb than at 850 mb. The fact that cooling at 500 mb occurs in all the quadrants where the stability

Table 2

Values of the factor K (m/mb)

Wavelength (km)	PRIOR to Deepening									
	Grand Mean		Left Forward		Right Forward		Left Rear		Right Rear	
	dry	moist	d	m	d	m	d	m	d	m
2000	17	8	17	11	18	8	14	7	17	6
3000	7	4	8	5	8	4	6	3	8	3
4000	4	2	4	3	5	2	3	2	4	1
	AFTER Deepening									
2000	14	8	16	9	14	7	14	9	13	6
3000	6	3	7	4	6	3	6	4	6	3
4000	4	2	4	2	3	2	3	2	3	1

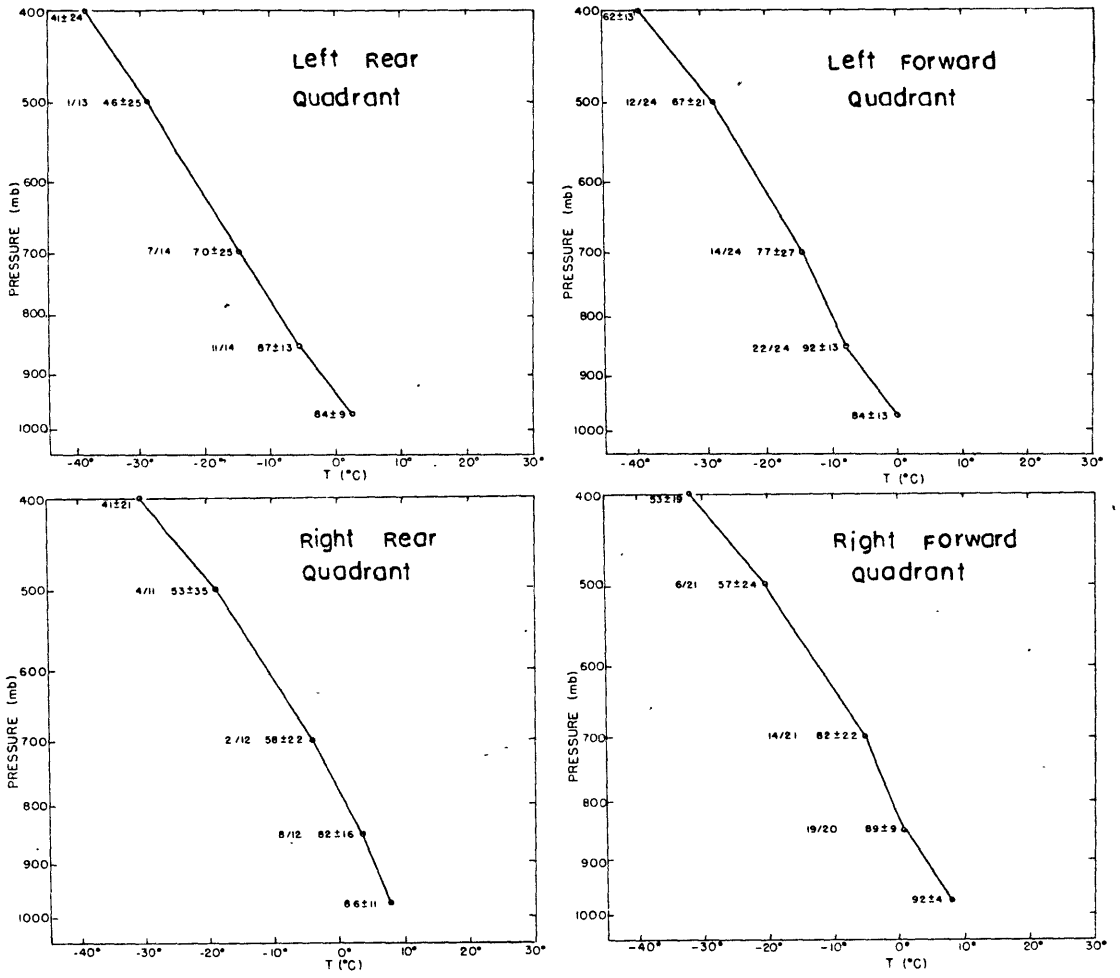

Fig. 13a. Mean sounding for "before" deepening cases derived from the information contained in Figure 11 and 12. The numbers on the charts indicate the means and standard deviations of the relative humidity at that particular level.

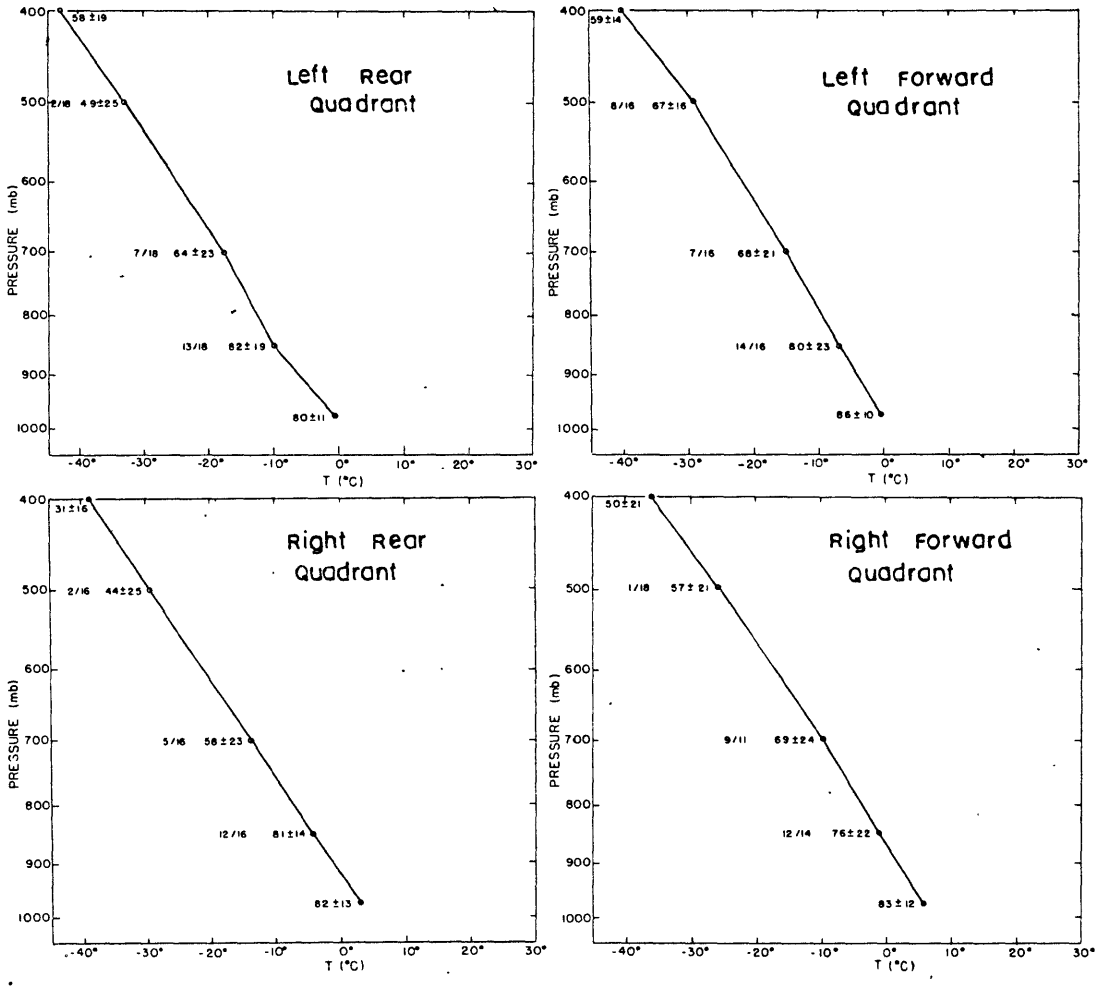
Left Rear Quadrant
Left Forward Quadrant
Right Rear Quadrant
Right Forward Quadrant
PRESSURE (mb)
T (°C)
400
500
600
700
800
900
1000
-40°
-30°
-20°
-10°
0°
10°
20°
30°
58±19
2/18 49±25
7/18 64±23
13/18 82±19
80±11
59±14
8/16 67±16
7/16 68±21
14/16 80±23
86±10
31±16
2/16 44±25
5/16 58±23
12/16 81±14
82±13
50±21
1/18 57±21
9/11 69±24
12/14 76±22
83±12

Fig. 13b.

decreases, while slight warming at 850 mb is only observed in one of these quadrants, seems to preclude sensible heat transfer from the ocean as being the only process involved. Indeed, heating from the ocean would likely be most important to the rear of the storm where the colder air is heated strongly from below by the relatively warm ocean waters. The movement of the storm toward warmer, less stable air in its later stages might be a factor. The fact that the air itself cools with time is most likely due to increased upward motion ahead of the storm. The component of upward motion from the low center eastward to the downstream high increases with increasing cyclonic vorticity of the low. Thus, since the magnitude of this component of ω (ω_2) is generally greater at 500 mb than at 850 mb in this model (see figure 1), the ω_2 increase would tend to stretch and destabilize the lower troposphere. Since extratropical cyclones are generally observed to move in a northeastward direction, this destabilizing effect would occur in the three quadrants mentioned above. The right forward quadrant, where we have the most confidence in the reality of a stability decrease, is also the quadrant where the ω_2 effect is the greatest (assuming the storm moves toward the northeast). Of course, the other effects mentioned above probably also play a role in the destabilization of the layer.

Figure 13 further indicates a drying trend in the two forward quadrants at both 850 mb and 700 mb. We have particularly good statistical confidence (better than the 5% significance level) of this on the basis of our sample at 850 mb. This effect appears to be the result of dryer air intruding around to the eastern side of the storm in its later stages of life, as is indicated by standard cyclone development models (see Pettersson, 1956).

V. Analysis Problem

We now wish to proceed with documentation of the analysis problem inherent in maritime areas, via two explosive oceanic cyclone cases. As discussed by Sanders (1976), independent analysis of the surface and upper levels are mainly carried out with the aid of weather ship observations for the former areas, and aircraft readings for the latter region. Thus, a discovery of a small, relatively intense low over the ocean combined with an unrealistically smooth upper-level height contour pattern (because the density of the aircraft observation is not sufficient to discern the small-scale features associated with the surface cyclone) will generally imply the thickness pattern showing an excessively intense warm ridge near the surface storm. As we have seen from our diagnostic model, very little deepening would be predicted initially with the analysis. This same error may also be a reason that the NMC Primitive Equation (PE) model often falls short of predicting instances of explosive deepening found in maritime areas.

The problem could be eased if a more accurate thickness value over the surface low center could be found. Assuming that at some early time in the storm's life, we know the correct thickness over the low, we can find the thickness change over the center by using the expressions derived in the previous section for dry and moist processes, each with and without the frictional dissipation effect included.

The two cases involved are those of January 9-11, 1974, and February 4-5, 1975. Each of these North Atlantic Ocean Cases were marked by rapid intensification within a brief time period. In order to achieve the most accurate analysis possible at the surface and upper

levels, soundings from island stations, weather ships, and satellite observations obtained from the National Center for Atmospheric Research were utilized. Ships' logs were obtained from the National Climatic Center in Asheville, North Carolina so as to improve the surface data coverage in the surface analyses. Aircraft reports were utilized for wind data at upper levels. The Northern Hemisphere data tabulations were also used to supplement the coverage at the surface and aloft. Thus, with the additional aid of satellite photographs, surface analyses were obtained every six hours during the major portion of each of the storm's lives.

Once these analyses were completed, 1000 - 250 mb thermal winds were calculated and plotted along with the 1000 - 250 mb thickness values. The 250 mb level was chosen as a basis for these calculations, because this is the mandatory pressure level closest to the mean level of the aircraft observations. The procedure used for calculating the thermal winds involved assuming the aircraft winds (at approximately 250 mb) were geostrophic and finding the 1000 mb geostrophic wind at the corresponding location from the analyzed 1000 mb geopotential field.

Specific values of the 1000 - 250 mb thickness were obtained from our soundings, and were supplemented in sparse data coverage regions by satellites (NOAA II, SIRS-B) measurements of the 1000 - 250 mb thickness. The measurements were used at times within plus or minus three hours of the map observation. The technique for deriving the geopotential fields from the satellite derived vertical temperature profile involves statistical correlations between geopotential and temperature, and is explained in detail in Smith and Fritz (1969) and Smith et al (1970). Thickness values are simply taken from the geopotential

differences. Corrections are employed to account for the presence of clouds, high terrain, and strongly heated ground. These corrections are needed because perturbations due to variations in nongaseous absorbers (such as clouds) are not accounted for in the regression relations, the surface of the earth is assumed to be at a fixed pressure level (1000 mb) and the ground and shelter temperatures are assumed equal. It is also noted in Smith et al (1970) that the transmission functions on which the derived temperature profile is based, vary significantly with water vapor content, but this variation is generally explained as a function of temperature due to the high correlation of water vapor content with temperature.

Hayden (1971) has compared the relative accuracy of the SIRS geopotential data with traditional radiosonde observations, and has found that in situations where high clouds are not prevalent, geopotential heights given by SIRS are just as accurate as the radiosonde observation. Even in cases of no high clouds and intensive low tropospheric cloudiness, a reasonable value of the temperature (and thus, geopotential) can be obtained. This is because some of the best tropospheric temperature predictors in the regression equations are the lower stratospheric temperatures, which are generally quite accurate because of the lack of clouds in this area.

From Hayden's (1971) results, we would estimate that the satellite thickness values have an uncertainty ranging from 2 dm in clear situations to 10-12 dm in high cloud regimes. Regardless, we feel that the satellite data was of some value in supplementing our thermal winds and traditional radiosonde values.

Using the above data, we performed a thickness analysis every twelve hours during the times of these intense storms. We used these analyses as a check on our thickness change formulae, used in the previous section, except that now we are dealing with the 1000 - 250 mb thickness. Thus, we used similar arguments in deriving the thickness tendency equation similar to (50), except that we are assuming most of the adiabatic temperature changes to be taking place between 850 and 4000 mb by using our sounding samples to find $(\theta_{40} - \theta_{85})$ or $(\theta_{40} - \theta_{85}) - (\theta_{40} - \theta_{85})_{wet}$ whichever is appropriate. The value of $\overline{(T/\theta)}$ was also assumed to be a constant of .85 in the 1000 - 250 mb layer. The values are summarized in Table 3.

We note fairly good agreement between the thickness change over the low center predicted by the moist process with friction for the January case, although observed thickness change values over the center tend to be a bit more positive or less negative than our moist frictional process would predict. However, all four of our methods for the February case yield consistently "cooler" thickness changes over the center than is actually observed. We know that in the February case (contrary to the January case, and to what is normally observed), the storm moved toward colder air (as indicated by the 1000 - 250 mb thickness pattern). Thus, we would expect (and the theory predicts) large thickness decreases over the center.

Thus, especially in the February case, there must be some warming mechanism which the theory ignores. The most probable item is convection, perhaps initiated by strong sensible heat transfer from the ocean to the adjacent atmosphere. Checks of the ships' logs for those vessels located near the storm center for both cases, reveals warmer sea surface

Table 3

Calculated thickness change over the low center

		dry processes		moist processes	
	$\Delta h'$ observed (m)	with friction (m)	without friction (m)	with friction (m)	without friction (m)
	(Case of January 9-11, 1974)				
12Z, Jan. 9 - 00Z, Jan. 10	- 70	-306	- 45	-119	+ 22
00Z, Jan. 10 - 12Z, Jan. 10	+ 80	-133	+141	+ 31	+178
12Z, Jan. 10 - 00Z, Jan. 11	- 10	-125	+168	- 14	+157
	(Case of February 4-5, 1975)				
00Z, Feb. 4 - 12Z, Feb. 4	-190	-594	-439	-439	-356
12Z, Feb. 4 - 00Z, Feb. 5	-130	-603	-329	-308	-255
00Z, Feb. 5 - 12Z, Feb. 5	+ 60	-296	- 56	-211	- 70

temperatures than air temperature (on the order of 5°C). Yet, there is no indication of this difference being any larger for the February case than for the January case. Of course, the data coverage for February, 1975 at both the surface and aloft was not as good as for the January case, so the analysis of the thickness patterns, especially in the February case, was likely not as accurate as we would have liked.

VI. A Further Look at the Sounding Samples

Although we found no deep layers of conditional instability throughout our sampling of 140 soundings, we did look for individual cases of potential instability. Potential instability represents the "potential" for an atmospheric layer, if lifted as a whole, to become statically unstable. Although no mean potential instability for the entire sample in the before cases exists, an examination of individual cases showed a decrease of θ_w (or equivalently, θ_e) in the surface -850 mb layer in 6 of 39 cases in the two forward quadrants, where large scale ascent is likely to make any potentially unstable situations a reality. The two rear quadrants showed a larger percentage of potentially unstable surface -850 mb layer (9 or 25 cases). However, large scale ascent presumably does not occur in this region, so we do not believe any deep convection activity would break out here.

Only one case showed potential instability in the forward quadrants for the 850 - 700 mb layer. This case, incidentally, was potentially stable in the surface -850 mb layer. However, even though our soundings do not indicate any deep layers of conditional or potential instability, the possibility does exist for this to occur through processes on a shorter time scale than we are seeing. About twenty-four hours generally separates the "before" soundings from the "after" soundings.

Simpson (1969) has found evidence that deep convection plays a decisive role in the explosive deepening of oceanic cyclones. One possible reason for our sampling not indicating any deep layers of conditional instability is that the sample was taken mainly from cyclones out in the open waters of the Atlantic and Pacific oceans, and away from the

eastern coastlines of Asia and North America, where there are particularly good possibilities for strong sensible and latent heat transfer (see, for example, Manabe, 1957 or Bunker and Worthington, 1976) as a result of cold, dry continental air masses moving out over the relatively warm ocean waters. Simpson's (1969) study was based on data collected in the Gulf of Alaska, again just off the Alaskan and Canadian coasts.

VII. Application of the Model to the Two Oceanic Storm Cases

Finally, from our surface and 1000 - 250 mb thickness analyses, we obtained model parameters for each of the cases. So that we could employ an objective means by which the basic meridional temperature gradient $\underline{a}$, and the temperature perturbation $\hat{T}$ could be evaluated, we replaced the thickness analysis via a simple space averaging technique to achieve a "filtered" field of thickness, $\overline{h}$, where h represents the thickness. Thus, this latter $\overline{h}$ field, when subtracted from our original thickness field h, tells us the $(h - \overline{h})$ field, and thus, the temperature perturbation values for the individual case. These model parameters and the calculated tendencies are summarized in Table 4.

As we can see from the results, our calculations of geopotential tendency fall far short of the observed values, and we did not even consider the frictional filling effect. Values of the speeds are too high and the likely cause of this appears to be a liability of all quasi-geostrophic models, that is the intensity of vertical motion centers is generally too concentrated, thus resulting in greater divergence effects, and overestimates of the horizontal gradient of geopotential tendency and thus the speed. Krishnamurti (1968) has found in a balance model that divergence and deformation effects are the likely cause of this problem.

The underestimate of the observed explosive deepening is likely to be caused, among other things, by an underestimate of the actual temperature gradients. Our model would likely predict more deepening if we had accurate estimates of the thickness gradients in the lower troposphere

Table 4

Calculations of Model Parameters

Quantity	Units	January, 1974			February, 1975		
		1/9 12Z	1/10 00Z	1/10 12Z	2/4 00Z	2/4 12Z	2/5 00Z
L	km	2908	3260	2954	3400	2222	2554
a	°C/100 km	1.50	0.96	0.65	1.37	1.29	1.05
$\hat{T}$	°C	2.35	2.35	2.60	1.05	2.50	3.46
f_o	10^{-5} sec^{-1}	10.8	11.0	11.5	9.0	9.6	10.7
β	10^{-5} sec^{-1}	3.1	3.1	4.3	1.6	6.7	6.8
η_0	10^{-5} sec^{-1}	13.9	14.1	15.8	10.6	16.3	17.5
λ/L	-	.12	.095	.094	.07	.10	.095
(γ moist from our sounding sample)	-	.063	.063	.057	.063	.063	.057
$\eta_0/T_0\gamma$	10^{-6} sec^{-1} °K^{-1}	8.8	8.9	11.1	6.7	10.3	12.2
central p	mb	973	949	934	999	965	935
model central $\partial p/\partial t$	mb/12 hr	-6.4	-3.1	-2.7	-1.3	-5.5	-5.7
model speed	kts	59	39	26	53	47	42
observed speed	kts	29	26	14	33	36	25
actual central $\partial p/\partial t$	mb/12 hr	-24	-15	+6	-34	-30	+8

(say, from 1000-500 mb), as we examine the 1000-250 mb thickness patterns, we are likely seeing the effects of the temperature gradient damping off rapidly in a thin layer above 500 mb. If we had used the original version of the model, a simple amplification of the tropospheric thickness patterns to conform to the $(1 - \alpha \ln \frac{p_0}{p})$ vertical dependence would have helped. Yet, we are faced with the fact that the vertical structure of the horizontal temperature gradients over the ocean likely looks more like our pressure independent structure at least in the lower half of the troposphere with rapid damping of the gradient occurring in the upper troposphere, or perhaps, even an entirely different temperature configuration in the upper troposphere.

We have also looked into the possiblity that our model underestimates the effects of the thermal vorticity advection aloft. We calculated this effect directly from our mean thermal wind field and our $(\bar{h} - h)$ field and compared this with a corresponding expression in the model for PTVA, and found that any discrepancies are small enough to produce a negligible effect on the deepening calculations.

We have already mentioned the possibility of convection playing a role in the development of the storm. Our model also takes no account of the sensible heat transfer, although the former effect of latent heat transfer due to convection has the potential to be far more important.

We must also question the applicability of quasi-geostrophic theory to those intense maritime storms. Perhaps an exhaustive effort to gather significantly more data over the ocean for a finite period of time could be used to perform a study similar to that of Krishnamarti (1968) to partition the various geostrophic and non-geostrophic effects on the vertical

motion. A study of this kind might enable us to understand better the physical processes in these storms.

VIII. Summary and Conclusions

A new quasi-geostrophic diagnostic model has been developed to conform to a postulated temperature structure over extratropical maritime regions. We have found that vertical motions tend to reach maximum values at higher levels than was found in the earlier (Sanders, 1971) model. We also found that preferred wavelengths for deepening were a bit higher in the new version, due to the increase in vertical extent of strong baroclinicity. Perhaps the major advantage of this model over the original one is that we have a diagnostic calculation of temperature perturbation intensification for deepening cyclones. This is especially important since it is the temperature perturbation which is necessary for storm intensification to occur. In addition, a more physically appealing frictional formulation ahs been derived, which contains the physical effects of frictional dissipation and divergence throughout the troposphere. Also, the desirable effects of the frictional parameterization used in Sanders' model have been retained (i.e., the short-wave cutoff, and the limiting intensity beyond which $\hat{\zeta}_4$ dominates $\hat{\zeta}_1$). We feel that perhaps, friction is an important mechanism for cutting off cyclone growth in maritime regions because of the very strong observed circulations which, according to our theory, become so intense that the friction will cause a cessation of deepening. Rather good success has been achieved in predicting thickness changes over storm centers over land (where this data sample is quite adequate) by combining Sanders' (1975) formulae and our frictional expressions. More modest success was found in attempting to use these formulae over the oceans, possibly because of poor data coverage, and an ignorance of

just what the value of $\frac{c_d V_0}{\Delta z}$ is over maritime areas.

An extensive sounding sample has been taken over regions under the influence of intense oceanic storms. Though we found no direct evidence for convection occurring, ruling out this possibility was determined to be an error, for potential instability was found to exist in some cases, and the time intervals between map times might be inadequate to fully support the contention that convection does not occur at some timd during the explosive deepening of oceanic storms.

As noted above, in reference to thickness changes experiments. two cases of explosive cyclogenesis over the North Atlantic were examined. Our sounding sample was used as a basis for evaluating model parameters, and to find deepening tendencies. It was found that these two cases that even without friction, observed deepening rates vastly exceeded those tendencies computed with the aid of the model. The reasons for this failure, as has been discussed earlier, may have been due to a neglect of non-geostrophic effects, sensible heat transfer or convective activity, lack of an adequate representation of the temperature structure, or lack of data causing analysis errors.

We feel that we have achieved a degree of success in capturing some of the synoptic scale physical effects of large-scale temperature and vorticity advections in the development of oceanic cyclones. Although our sounding sample reveals generally very small static stability of air in the vicinity of these waves (when we refer to a saturated atmosphere), even this small stability is not sufficient to account for the explosive deepening of these storms. Lack of adequate data and an essential ignorance of the physical processes of these storms is a

likely factor slowing our progress in being able to predict such large deepening tendencies. The above factors are inevitably tied together. Once a network has been set up to evaluate the three-dimensional structure of temperature, moisture, and winds in maritime areas, adequate tests of the physical processes mentioned above may be made.

References

Bunker, A.F., and L.V. Worthington, 1976: Energy exchange chart of the North Atlantic Ocean. Bull. Amer. Meteor. Soc., 57, 670-678.

Cressman, G.P., 1960: Improved terrain effects in barotropic forecasts. Mon. Wea. Rev., 88, 327-342.

Haltiner, G.J., 1971: Numerical Weather Prediction. John Wiley and Sons, Inc., 314 pp.

Hayden, C.M., 1971: On reference levels for determining height profiles from satellite-measured temperature profiles. NOAA Tech. Mon. NESS 32, 15 pp.

Krishnamurti, T.N., 1968: A study of a developing wave cyclone. Mon. Wea. Rev., 96, 208-217.

Manabe, S., 1957: On the modification of air-mass over the Japan Sea when the outburst of cold air predominates. J. Meteor. Soc. Japan, Series II, 35, 311-325.

Palmen, G., and C.W. Newton, 1969: Atmospheric Circulation Systems. Academic Press, 603 pp.

Petterssen, S., 1956: Weather Analysis and Forecasting. Second Edition, Vol. I, McGraw-Hill, 428 pp.

Sanders, F., 1971: Analytic solutions of the non-linear omega and forticity equations for a structurally simple model of disturbances in the baroclinic westerlies. Mon. Wea. Rev., 99, 393-407.

_____, 1976: The effect of incorrect initial analysis on the predicted deepening of oceanic cyclones. Paper delivered at the Sixth AMS Conference on Weather Forecasting and Analysis, May

10-13, 1976, Albany, N.Y.

Smith, W.L., and S. Fritz, 1969: On the stratistical relation between geopotential height and temperature-pressure profiles. ESSA Tech. Mon. NESCTM 18, 16 pp.

Smith, W.L., H.M. Woolf, and W.J. Jacob, 1970: A regression method for obtaining real-time temperature and geopotential height profiles from satellite spectometer measurements and its application to Nimbus 3 "SIRS" observations. Mon. Wea. Rev., 98, 582-603.

Simpson, J., 1969: On some aspects of air-sea interaction in middle latitudes. Deep-Sea Res., 16 (Supplement), 233-261.